Evaluation of organic perovskite photoconductors for x-ray imaging detectors

Dhilippan Mamsapuram Panneerselvam

A Thesis

in

the Department

of

Electrical and Computer Engineering

Presented in Partial Fulfillment of the Requirement

for the Degree of Master of Applied Science at

Concordia University

Montréal, Québec, Canada

August 2017

CONCORDIA UNIVERSITY

SCHOOL OF GRADUATE STUDIES

This is to certify that the thesis prepared

By: Dhilippan Mamsapuram Panneerselvam

Entitled: Evaluation of organic perovskite photoconductors for x-ray imaging detectors

and submitted in partial fulfillment of the requirements for the degree of

Master of Applied Science

Complies with the regulations of this university and meets the accepted standards with respect to originality and quality.

Signed by the final examining committee:

_____ Chair

Dr. Robin Raut

_____ Examiner, External

Dr. Anjan Bhowmick (BCEE)

_____ Examiner

Dr. Steve Shih

_____ Supervisor

Dr. M. Z. Kabir

Approved by: _____

Dr. W. E. Lynch, Chair
Department of Electrical and Computer Engineering

_____20_____

_____
Dr. Amir Asif, Dean
Faculty of Engineering and Computer Science

Abstract

Evaluation of organic perovskite photoconductors for x-ray imaging detectors

Dhilippan Mamsapuram Panneerselvam

Research over organic perovskites for light harvesting gained the momentum in past decades. Due to the convenient low temperature and uniform deposition over large area these materials are being tested for the vitality in various light harvesting devices such as in solar cells, X-ray detectors, gamma photon captures etc., On meeting the expectation, the power conversion efficiency in these devices peaked above 20% in around four years of research. But the underlying physics in these materials remains a mystery particularly that which concerns the undesirable high dark currents and photo gains when illuminated with X-ray for medical imaging.

In this thesis, the x-ray sensitivity of perovskite photoconductors under different detector operating conditions has been identified. The primary mechanism that regulates the photocurrent and dark current behavior of X-ray imagers based on organic perovskite photoconductors has been identified. Energy level misalignments between different layers of X-ray imagers leading an injective photo-gain has been investigated. The signal spreading due to trapping, k-fluorescence generation and reabsorption, pixel aperture and primary charge interaction with photoconductor has been accounted by calculating the theoretical MTF for different spatial frequency. These imaging performances are also explored by calculating the theoretical Detective Quantum Efficiency (DQE) at zero spatial frequency. Proceeding further, numerical investigation of organic perovskite had also been accounted to visualize the electric field profiles along the thickness of photoconductor. All possible recombination mechanisms and tr aps are included in the numerical solution of continuity, trap, and Poisson's equations simultaneously. Sensitivity reduction due to repeated exposure (Ghosting) has been investigated. A variation of electric field profile under different exposure levels has been noticed. It becomes evident that significant deviations between the analytical and numerical approaches were noticed under high exposure levels. This is due to the significant variation of electric field profiles under very high exposures. The work in this thesis identifies the important factors such as the need for appropriate blocking contacts for low dark currents, improved carrier transport properties in perovskite films and proper energy level

alignment between different layers of photodetector in order to make successful perovskite x-ray detectors.

ACKNOWLEDGEMENT

My gratitude extends over this existence which made me a potential for the completion of this thesis work. Principally, I would like to express my earnest gratitude to my supervisor Dr. M. Z. Kabir for this motivation, encouragement, guidance and financial support throughout my thesis work. I am also grateful to my parents who supported me mentally through their thought provoking insights. I am also grateful to my colleagues Mr. Salman Moazzem Arnab and Mr. Kaveh Rahbardar Mojaver for their innumerable friendly discussions. I would also like to extend my gratitude to my colleague Ms. Nour Hijazi for help with COMSOL simulations. I am also grateful to Mr. Md Mesbahus Saleheem for his encouragements, and friendly advice. Finally, I would like to extend my gratitude to my lab mates named Ms. Sevin Samadi, Mr. Seyedamin Firouzeh, and Ms. Fatemeh Ahmadi.

With

meditative

awareness

Table of contents

Table of Figures

List of tables

List of Abbreviations

A/D	Analog to Digital
AMA	Active Matrix Array
FPD	Flat Panel Detector
TFT	Thin Film Transistor
Ag	Silver
Au	Gold
Gd_2O_2S	Gadolinium oxysulfide
CsI	Cesium iodide
$CH_3NH_3PbI_3$	Methyl ammonium lead iodide
$CH_3NH_3PbBr_3$	Methyl ammonium lead bromide
PEDOT: PSS	Poly polystyrene sulfonate
PCBM	Phenyl-C_{61}-butyric acid methyl ester
ZnO	Zinc oxide
VB	Valance Band
CB	Conduction Band
HOMO	Highest Occupied Molecular Orbit
LUMO	Lowest Unoccupied Molecular Orbit
DQE	Detective Quantum Efficiency
MTF	Modulation Transfer Function
NPS	Noise Power Spectrum
LSF	Line Spread Function

Chapter 1: Introduction

1.1 X-rays

The innovation of X-rays on 1895 by Wilhelm Röntgen marks a landmark for medical diagnosis of internal organs. X-rays are electromagnetic waves which can be produced when electrons in the inner shell of a heavy atom are knocked out influencing the other electron from the outer shell to fill this space. This process initiates the formation of x-rays. The produced x-rays have very short wavelength (~nm) correspondingly larger energy. The unit of X-ray exposure is Roentgen (R) in CGS systems while it has a unit of Gray (Gy) on modern SI system. Exposure establishes the ability of X-ray to ionize the air. X-rays are mainly used in imaging of internal organs and luggage scans.

1.2 X-ray imaging

X-rays encounters different attenuation for different materials. This lays the basis of X-ray imaging in medical diagnosis. Depending upon the attenuation encountered on different body parts, it forms a gray image for tissues, white for bones, and complete black images are obtained for air [1]. The X-ray imaging has also seen an evolution. As such there can be two different types of X-ray imaging techniques as Analog imaging technique and Digital imaging technique.

1.2.1 Analog X-ray imaging

An analog X-ray medical imaging uses photographic plates to record the images. These photographic plates require chemical treatments to develop the images for diagnosis. According to this process, the patients have been positioned appropriately between the X-ray tube and photographic plate and exposure to x-rays are made. After the exposure of radiations, the photographic plates are removed for post processing to develop the images. This process is time-consuming as an ample time span is necessary to develop the image from photographic plates. Furthermore, the probability that an appropriate image can be developed from these techniques is low as it requires careful chemical processing of the films in dark rooms [2].

1.2.2 Digital X-ray imaging

The limitations of the analog X-ray imaging have been overcome through the usage of digital imaging techniques. Here the images are formed instantaneously through the usage of X-ray detectors, modern computers and image processing schemes. Better-quality images of the internal organs can be developed with minimum dose deposition on patients through this technique. In this technique, an X-ray detector (solid state device), and Active Matrix Arrays (AMA) are used. The AMA is a 2-dimensional arrangement of many pixels. Each Pixel consist of a storage capacitor, A/D converters and thin film transistors A/D converters are essential for interpretation of the analog signal that is formed in imagers, to digital information. Thin film transistor (TFT) is used as a switch to transfer the stored information of the image in capacitor for data processing. The photodetector in this method forms the basis for imaging. In photodetector, the attenuated x-rays (attenuated from the patient body) are absorbed and electron-hole pairs are generated. These electron-hole pairs constitute the data for the image. In recent days, the Flat Panel Detector (FPD) constituting an integrated package of the photodetector, thin film transistor, and A/D converters are conveniently made in an Active Matrix Array (AMA). Not all the photoconductor establishes a state where the electron-hole pairs are production through the direct absorption of the x-ray radiation. Based on the scheme used to produce electron-hole pairs the digital X-ray imagers are classified as direct conversion detector and indirect conversion detector.

1.2.3 Direct conversion X-ray detector

In direction conversion x-ray detectors, x-rays are made to fall directly on the photoconductor. The electron-hole pairs are generated in the photoconductor just after the x-rays are absorbed. Now the generated free electron-hole pairs can be collected. But the influence of the biasing of this type of detector plays a significant role in the charge collection. In Figure 1.1, the photoconductor is positively biased, as the top electrode is positive biased, electron moves to the top electrode and the hole are collected across the capacitor (C_{mn}) which is read using TFT. If the biasing is reversed electrons will be collected across capacitors. The selection of polarity for biasing the detector entirely depends upon the charge transport properties (mobility and lifetime) of the underlying photodetector. Resolution of the images formed by this method constitutes the main advantage of direct conversion detector over indirect conversion. An enhanced image resolution is possible in this scheme as the x-rays do not suffer from signal spread to adjacent

pixel, multistep processes for the creation of electron-hole pair is avoided, and the addition of noise in the signal is also limited due to direct formation of electron-hole pairs. Furthermore, the number of layers required in the fabrication of the detector also less.

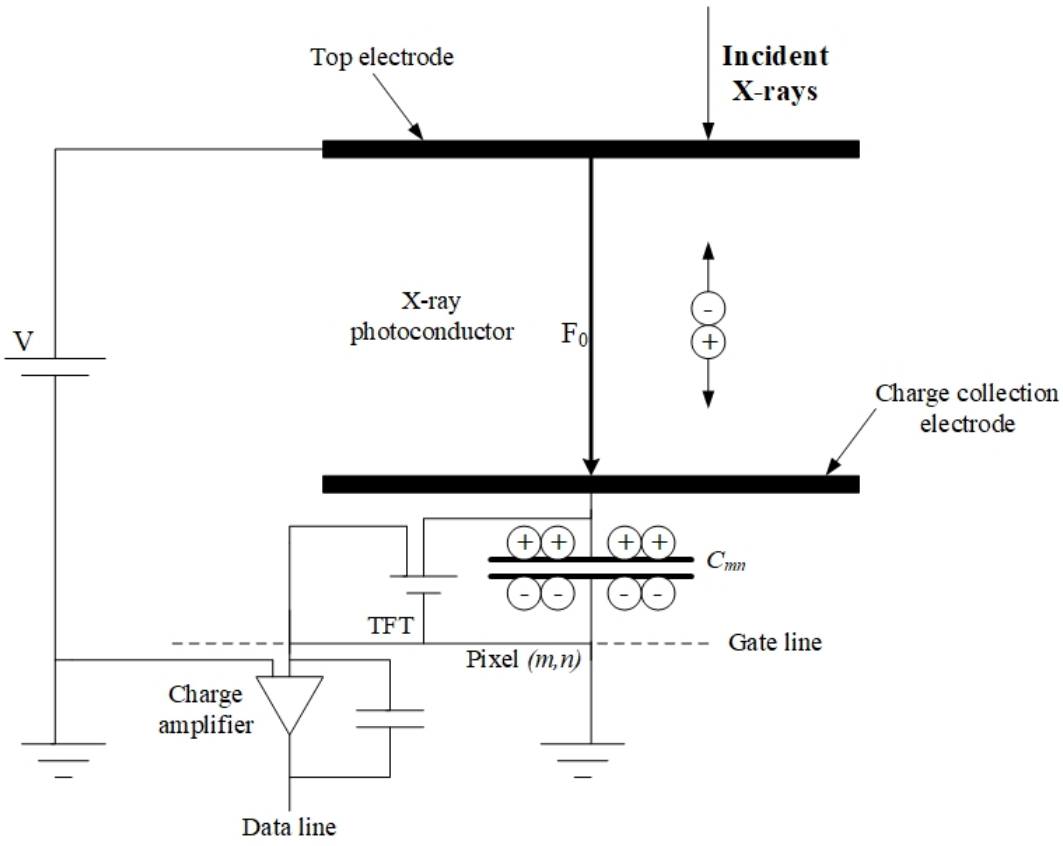

Figure 1.1: Simplified diagram of the direct conversion X-ray digital imaging detector (only one pixels is shown) [3 ,4]

1.2.4 Indirect conversion X-ray detector

Indirect conversion is another method employed to mount the image from an object. Here the scintillators play a major role in the conversion of incoming x-ray radiations to light photons as shown in Figure 1.2. These generated light photons are then absorbed by the photoconductor on the AMA. After absorption, the conventional process takes place in which the data (charge collected) in the capacitors are read appropriately using the external peripheral circuitry. Practically either gadolinium oxysulfide (Gd_2O_2S) or cesium iodide (CsI) is used as scintillators for indirect conversion x-ray imagers. Normally indirect conversion x-ray imaging is not preferred

over direct conversion because the resolution of the images formed are poor and the light photon generated in scintillators tend to spread toward the adjacent pixel and cause blur [2].

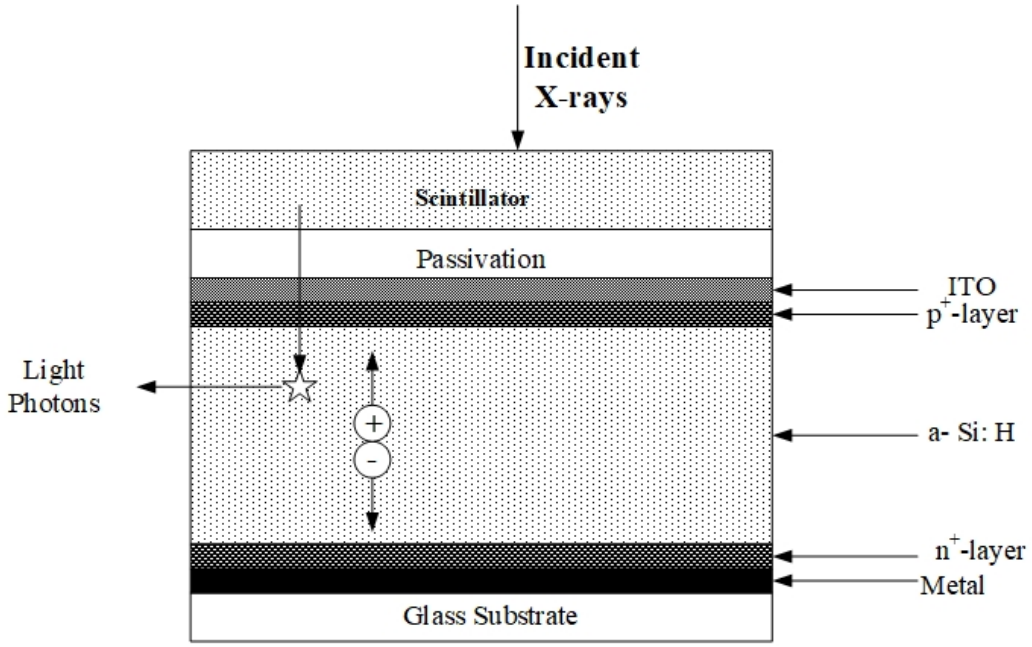

Figure 1.2: Simplified representation of indirect conversion digital X-ray detector (only single pixel is shown)

1.3 Image readout

Figure 1.3, shown the image readout scheme for a group of pixels. Here Thin Film Transistors (TFT) are used in the readout mechanism. All the TFT's gate terminal are connected for the trigger, while the data points are conveyed through the source terminal. When the gate terminals in 'm' row is activated this will enable all the TFT in 'm' row and the data will be relayed parallel to the multiplexer. This process continues to all the rows as m, m+1… Hence all the data of images are read and relayed to a computer for image construction.

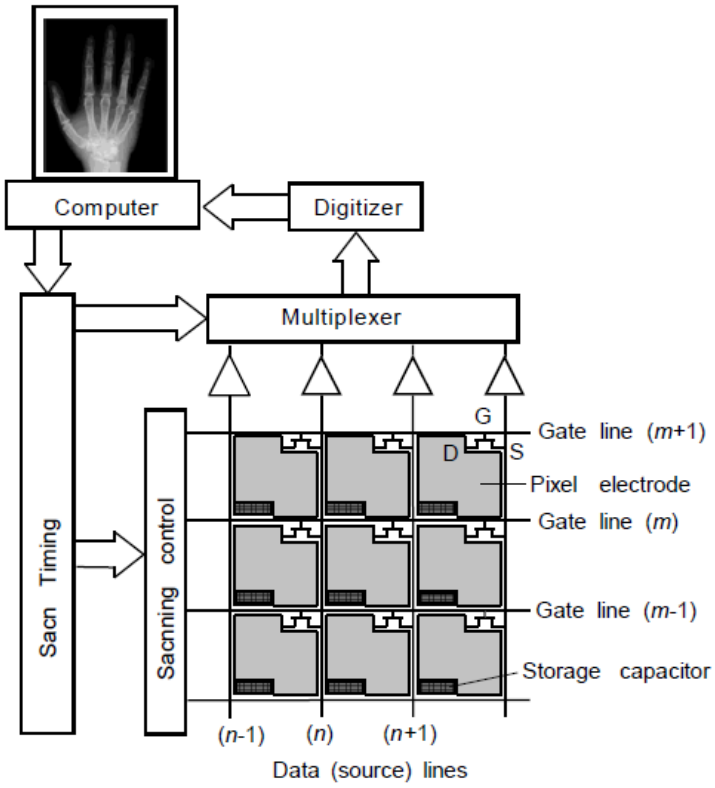

Figure 1.3: Electronic readout scheme used for image data readout from pixels [2]

1.4 Research Motivation

1.4.1 Problem Identification

With the present state of the art, most of the modern flat panel X-ray imaging systems are dominated using a-Se (amorphous selenium) as a photoconductor because of its low dark current, reasonable carrier transport properties and convenient deposition over a large area. But a-Se fails to establish an ideal performance in many instances. Though the achievable sensitivity in the a-Se based imager is significant and suitable for imaging, it has low conversion gain. Low conversion gain corresponds to the inability of the material to produce sufficiently large electron-hole pairs when X-rays are illuminated. Furthermore, the electron-hole pair creation energy ($W_{\pm}$) has a strong dependence on applied electric field (F) as,

$$W_{\pm} = W_{\pm}^{0} + \frac{B(E)}{F^{n}} \qquad (1.1)$$

where $W_{\pm}^{0}$ is the electron-hole pair creation energy at the infinite electric field which can be obtained through the relation $W_{\pm}^{0} = CE_g + E_{phonon}$ (E_{phonon} is the phonon energy , E_g is the bandgap energy of material and C is a constant with values 2.2 [38] and 2.8 [38] for amorphous and crystalline materials respectively), $B(E)$ is an energy dependent constant term, and 'n' is an integer whose value lies in the range of 0.7-1 [22]. For enough free carrier generation, the required electric field becomes high (>10 V/μm). The high field also required for better charge collection and image readout. Adding to these facts, the drift mobilities of the carriers are also very low in this material. In a-Se, the hole mobilities are in the range of ~0.12 cm^2/V-s while the electron mobilities are in the range of ~0.003 cm^2/V-s. Relatively poor carrier transport properties can affect image resolution and temporal artifacts such as image lag and ghosting. Moreover, the main drawback of a-Se is its low X-ray sensitivity, which limits the imaging X-ray exposure or dose. Therefore, it has been a vital need to replace a-Se by a suitable photoconductor materials. Fortunately, recent publications ([26], [27], and [5]) show suitability of organic perovskite materials for X-ray photoconductor.

1.4.2 Excellency and perplexity of Perovskite – Present scenario

Organic perovskite materials establish a better attenuation coefficient under medical diagnostic X-rays on comparison with conventionally used a-Se. These materials can be conveniently deposited over a large area by cheaper solution processes. Furthermore, the electron-hole pair creation energy in these organic compounds are very low and in the range of ~5 eV. This electron-hole pair creation energy agrees well with the equation $W_{\pm} = 2.8E_g + E_{phonon}$ where the electron-hole pair creation energy can be defined as the average energy required from the incoming x-ray radiation to produce an electron-hole pair. The contributing parameter for this low electron-hole creation pair energy and better attenuation coefficient is believed to be from the lead halide (heavy element mixture) compounds in these materials. Moreover, the electric field required to drift the carriers across the organic perovskite photoconductors is much less compared to a-Se detectors. This is because of the superior charge transport properties of electron and hole in both polycrystalline films and single crystal structures. However, research on perovskite materials for X-ray detectors is at very premature level. There are lots of challenges such as finding suitable

detector structure for low dark current along with high sensitivity, resolution and better signal to noise performance.

1.5 Research objective

The objective of this thesis is to evaluate and establish the scope of perovskite materials in X-ray medical imaging. Hence this includes the research tasks as follows,

- Evaluating X-ray performances such as X-ray sensitivity, resolution, Detective Quantum Efficiency (DQE) of perovskite photoconductors using analytical models.
- Developing a suitable numerical model to determine the limits of the established analytical models and to examine the sensitivity reduction under repeated exposure.
- Investigating the origin of some unexpected detector phenomena such as excess carrier injection and dark current.

1.6 Summary

In this chapter, the essential of X-ray imaging and image readout are discussed. Towards the end, the research motivations are discussed along with my research objective. This thesis work is divided into five chapters. The first chapter governed the initial introduction of X-ray imaging and research motivation. The second chapter deals with the essential background theories of X-ray imaging, metrics of an ideal X-ray photodetector along with recently resolved charged transport properties of perovskite materials. Proceeding further, chapter three deals with the analytical evaluation of perovskite materials for X-ray imaging. Numerical evaluation of organic perovskite materials has been made in chapter four. Further scope of this material in X-ray imaging has been highlighted in chapter five.

Chapter 2: Literature review and theories

In this chapter, the properties of organic perovskites, and essential parameters that qualify an X-ray imaging detectors have been discussed. Moreover, vital conditions a photodetector must possess to qualify for X-ray medical imaging has also been discussed.

2.1 Properties of Perovskite

2.1.1 Composition and structure of Perovskite

The first ever observed Perovskite compound was calcium titanate ($CaTiO_3$) by German mineralogist Gustav Rose on 1839 [6]. Over the evolution of time, research in the field of optoelectronics concerns the usage of organic perovskite compounds [6], [7]. These organic perovskite materials have the chemical composition ABX_3, where *A* is the organic cation as $CH_3NH_3^+$ (methyl ammonium) or $NH_2CH_3NH_2^+$ (formamidine), *B* is usually a divalent metal ion either pb^{2+} or Sn^{2+}, and *X* is the monovalent halogen atoms as Cl^- or Br^- or I^-. The atomic arrangement consists of the organic cation (*A*) occupying all the eight corners of the unit cell, the divalent metal ion (*B*) is located at the body center of the unit cell, and the monovalent halogen ions (*X*) are located at the face center of the unit cells.

Numerous possible perovskite materials can be formed by varying the *A*, *B*, and *X* elements in perovskite composition ABX_3. But $CH_3NH_3PbX_3$ perovskite material, where $X = I^- or Cl^- or Br^-$ has been of special interest in optoelectronic research because of their high carrier mobilities, low charge recombination in bulk and low-temperature fabrication [8]. Recent review [9], highlighted a sharp increase in the power conversion efficiency of these materials in less than a decade which concludes that $CH_3NH_3PbI_3$ is the best candidate for optoelectronic research.

2.1.2 Band gap energy, *Eg*

Band gap energy can be defined as the difference in energy levels between the top of the valence band to the bottom of the conduction band. An insight on band gap, results in minimum amount of energy required, from the exciting radiations, to excite an electron from the valence band to the conduction band.

The band gap energy of complex three-dimensional perovskite structure ($CH_3NH_3PbI_3$) observed though density function theory deduces an energy band gap of ~1.6 eV [10]. The observed band gap of $CH_3NH_3PbI_3$ is comparable with other organic perovskites, as given in Table 2.1 below, by substituting halogen (X) atom.

Table 2.1: Comparison of band gap energy *(E_g)* of various organic perovskite materials which are in the present state of art in optoelectronic research [8, 10]

Perovskite compound	Band gap (E_g)
$CH_3NH_3PbI_3$	~1.6 eV
$CH_3NH_3PbBr_3$	~2.34 eV
$CH_3NH_3PbCl_3$	~3.11 eV

2.1.3 Charge carrier lifetime *(τ)* and mobility *(μ)*

The charge carrier lifetime (τ) is defined as the average time a carrier take to recombine and becomes unavailable for conduction. The mobility (μ) can be defined as velocity attained by the carriers per unit electric field. The product of mobility and lifetime ($\mu\tau$) determines the external electric field required for efficient charge collection in each optoelectronic application.

Although a long range of charge transport has been reported for $CH_3NH_3PbI_3$ perovskite [11], with the present state of the art of these materials, the mobility and lifetime depend upon the deposition techniques, nature of the film formed and the structure of the photodetectors. Considering these phenomena's, the mobility and lifetime of various organic perovskite films can be summarized in

Table *2.2*.

Table 2.2: Comparison of charge carrier mobility and lifetime in various organic perovskite compounds [12]

Perovskite compound	Mobility ($cm^2V^{-1}s^{-1}$)	Carrier lifetime (μs)
$CH_3NH_3PbI_3$ (Polycrystalline)	~1-10	~0.01-1
$CH_3NH_3PbI_3$ (Single crystal)	~24-105	~0.5-1
$CH_3NH_3PbBr_3$ (Polycrystalline)	~30	~0.05-0.16
$CH_3NH_3PbBr_3$ (Single crystal)	~24-115	~0.3-1

2.2 Essential parameters defining an X-ray photodetector

2.2.1 X-ray Sensitivity

X-ray sensitivity can be defined as the charge collected per unit area per unit exposure of radiations,

$$S = \frac{Q}{AX} \tag{2.1}$$

where Q is the collectible charge (C), A is the area of the photoconductor (cm^2), and X is the exposure level of incident radiation (R). Thus, the unit of X-ray sensitivity is $C/cm^2/R$. The exposure levels can also be conveniently defined in terms of SI unit as Gray, Gy (J/kg). 1 Roentgen of exposure can be defined as,

$$1\ R = 2.58\times10^{-4}\ C/kg = 0.00876\ J/kg = 8.76\ mGy$$

The experimentally obtained sensitivity of perovskite X-ray imagers are 25 $\mu CmGy_{air}^{-1}cm^{-3}$ for $MAPbI_3$ polycrystalline films and 80 $\mu CmGy_{air}^{-1}cm^{-2}$ for $MAPbBr_3$ single crystal films. It is

evident from these values of sensitivity that it is comparable with the values of sensitivity obtained from conventionally used a-Se detectors.

2.2.2 Photo-gain

When the X-rays are absorbed on the photoconductor (perovskite) it results in the creation of electron-hole pairs. These electron-hole pairs are separated and drifted to appropriately biased contacts. The drifting carriers constitute the current both under illumination as well as in dark. But recently many researchers [13,14, 15 and 16], have demonstrated that in photodetectors based on perovskite there is an undesirable gain which is either due to injection or tunneling of carriers from metal contacts.

One possible hypothesize about the origin of this gain is the presence of interfacial traps in metal-semiconductor interfaces. The existence of these interfacial traps is argued due to the presence of Pb^{2+} ions in perovskite films [17]. These ions at the interfaces create an ohmic interface which favors the injection of carriers. One possible solution to this problem is to modulate the concentration of Pb^{2+} ions during the preparation of perovskite films.

Another promising postulate for the origin of gain is the nature of films formed, by various deposition techniques used in the fabrication process of photodetectors. Films deposited by spray coating technique shows a superior gain. While the films deposited via spin coating shows a negligible or no gain during the operation of the photodetector. These are due to the formation of compact and dense films by spin coating while porous or less dense films by spray coating technique [15, 16]. Remarkably the nature of films brings out a short circuit between different layers. It is understood that a short circuit between glass (electrode) and photoconductor principally constitute the gain (injection) during the operation of the photodetector [15, 16]. It is also thought-provoking to note here that; the gain is a slow process and it establishes an onset time for it to take place. Furthermore, the gain also depends upon the operating temperature of the photodetector.

Figure 2.3 shows the energy band alignment of practically proven perovskite-based X-ray imagers. From the above theories, it becomes evident that injection of carriers in this photodetector takes place from metal (Ag) to photoconductor (Perovskite). Further theories of gain associated

with this perovskite-based x-ray detectors have been explained and the photocurrents are fitted with experimental results in section 3.3.3.

2.2.3 Detector Structure

The practically proven X-ray detector using polycrystalline $MAPbI_3$ has the structure as shown in Figure 2.1. Although a blocking layer (ZnO) is present to avoid any undesirable injections of carriers, there was a huge injection of carriers in this device which can be accounted with improper design of various layers or due to the usage of very high biasing potential (~7V) [26].

Figure 2.1: Structure of experimentally proven X-ray detector using polycrystalline $MAPbI_3$ perovskite [6,26]

Another approach using single crystal perovskite ($MAPbBr_3$) has also been demonstrated experimentally for imaging. This includes the structure as shown in Figure 2.2. It becomes curious to note that, during the operation of this device there was no undesirable photo-gain. This might be owed to the use of the relatively thick active layer (~2 mm) in comparison to other layers (few nm) of the detector and also due to the usage of very low biasing voltage (~0.1 V) [27]. Negligible or no gain state of this device is also observed in the theoretical calculation of photocurrent (Figure 3.5).

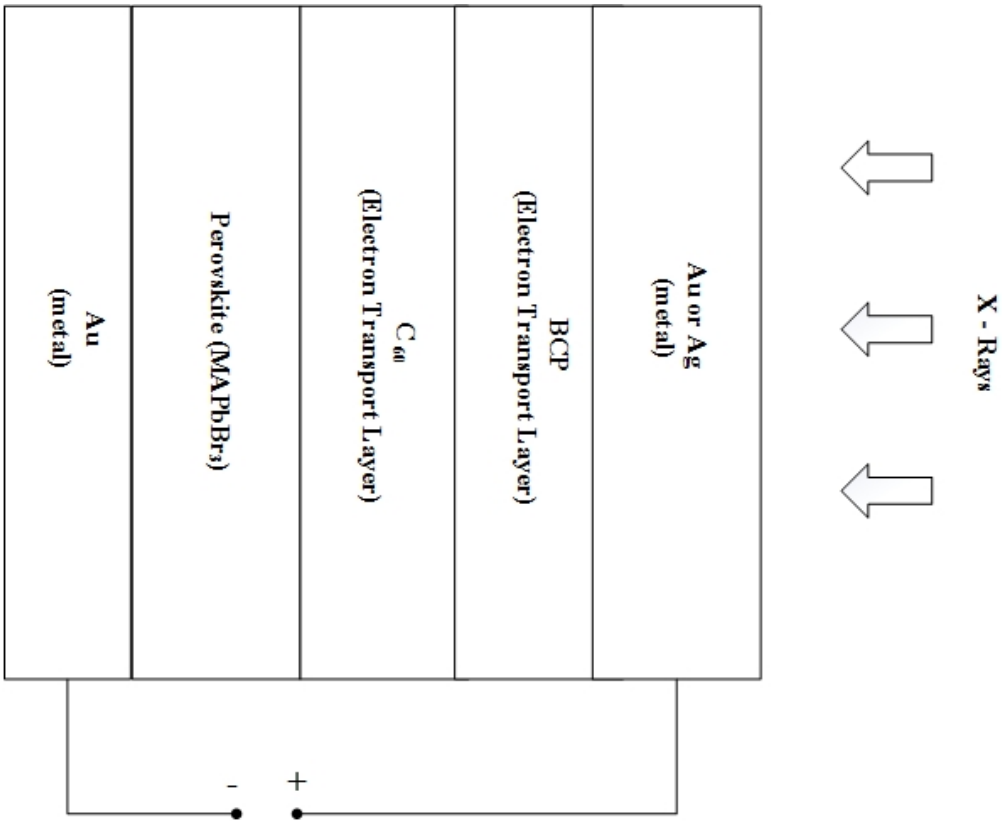

Figure 2.2: Structure of experimentally validated X-ray imager using single crystalline $MAPbBr_3$ [6, 27]

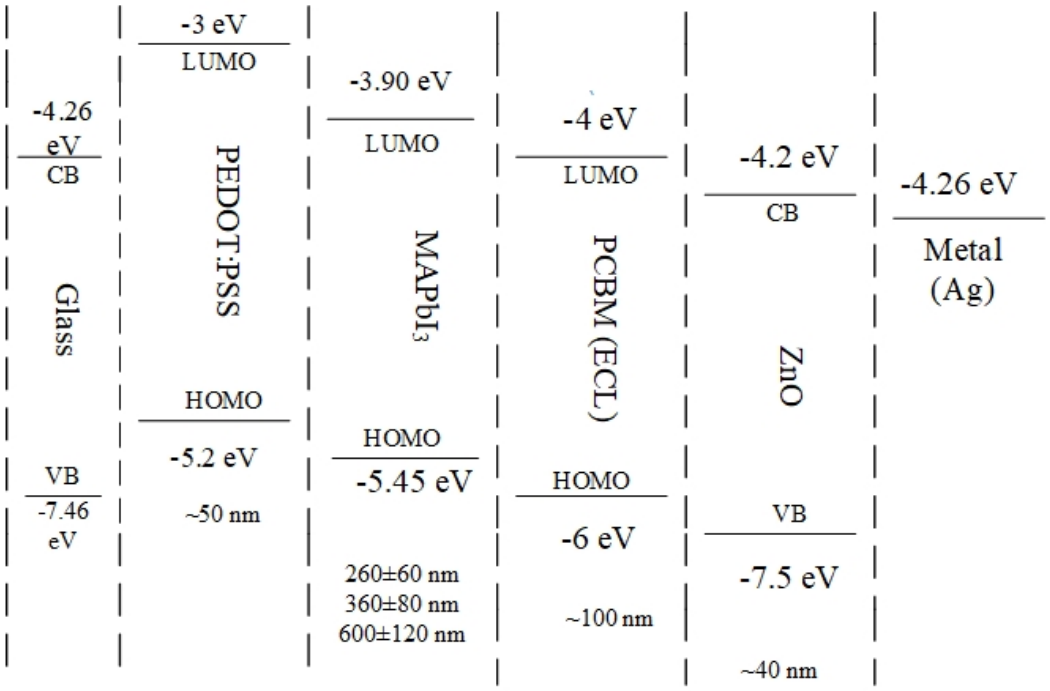

Figure 2.3: Energy level alignments between different layers in $MAPbI_3$ (polycrystalline) X-ray photodetector [6, 26]

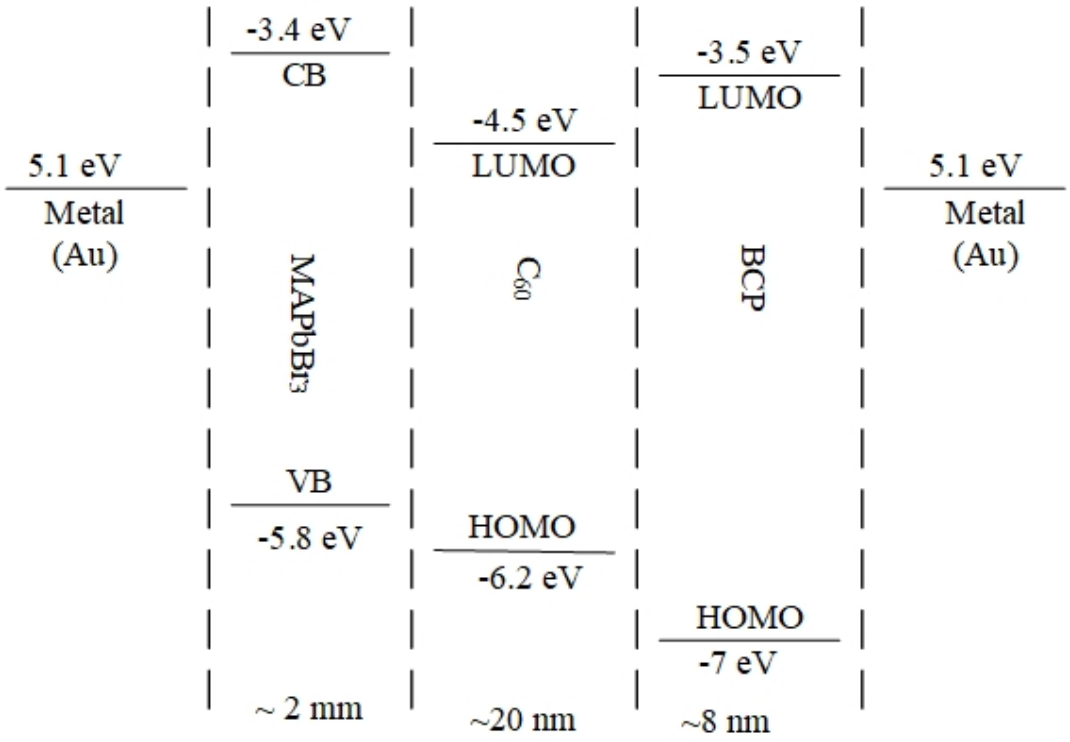

Figure 2.4: Energy alignment between different layers in $MAPbBr_3$ (single crystal) X-ray photodetector [6, 18, 19, 20, 27]

The charge transport in these devices can be visualized using these energy alignment diagrams. In Figure 2.3 and Figure 2.4, VB signifies Valence Band, CB signifies, Conduction Band, LUMO signifies Lowest Unoccupied Molecular Orbit, and HOMO signifies Highest Occupied Molecular Orbit.

2.2.4 Dark Current

An undesired current, after a biasing potential is applied across the photodetector without illumination, is termed as dark current. Injection of carriers from the metal contacts constitutes a chief mechanism for the origin of the dark current. An appropriate blocking contacts with larger bandgap and interface matching layers at metal/semiconductor interface may reduce the dark current. But the dark currents cannot be completely nullified due to some unbound charges. The origin of these unbound charges is still a factor for debate, as it might arise due to thermal generation of carriers from mid-bandgap of the semiconductors and it might also be associated with some material properties used in different layers of the detectors. Dark currents in the range of Femto to picoampere per mm^2 are considered as an optimum level in X-ray imaging detectors. An increase in the dark current above this range introduces image distortion or image blur in X-ray imaging detectors. But X-ray imagers based on perovskite shows dark current in the range of nano ampere. Hence investigating the mechanisms of the dark current has become vital in these detectors.

2.2.5 Modulation transfer function

Resolving ability of an imaging detector under different spatial frequencies can be conveniently expressed in terms of Modulation Transfer Function (MTF). It is the signal response of the imaging system accounting photo-conducting material used and the dimensions of the imaging system (pixel size). Superlatively, an MTF should reveal Fourier transform of the Point Spread Function (PSF) with respect to the spatial frequency. But due to the complexity associated with this transformation procedure a Fourier transform of the Line Spread Function (LSF) has been agreed as an expedient norm for MTF description of an imaging system.

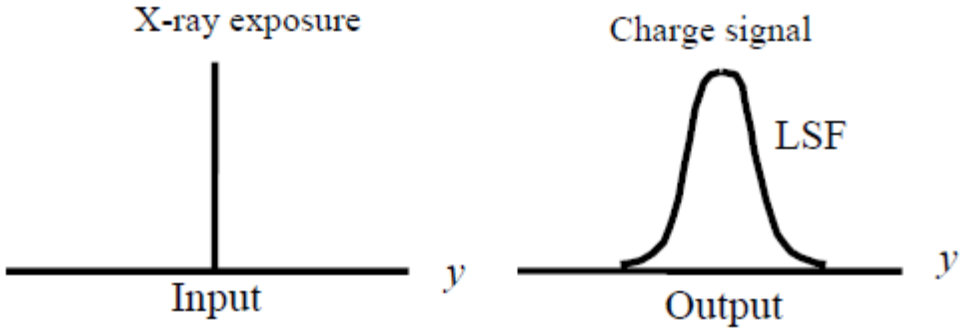

Figure 2.5: X-rays are incident upon the detector as a delta function while in the output has spread-out pattern of input, which corresponds to the Line Spread Function (LSF)

The dependency of MTF on detector material and dimension (pixel dimension) establishes a cascaded model for the calculation of a reliable MTF for imaging systems. Fundamentally the resolution distortion of the image that arises due to the size of the pixel and the arrange of it (pixel pitch). The MTF phenomena that arise out of it can be termed as aperture MTF (MTF_{ap}) which can be qualified with a sinc function of a pixel width. Secondly, the MTF arising from K-fluorescence reabsorption (MTF_k) becomes significant. This undesirable and unpredictable image distortion occurs due to the reabsorption of the secondary electron which has the energy corresponding to K-edge of the photoconductor. It has always been a metric of measure to have a closer MTF due to K-fluorescence with aperture MTF in imaging systems. Other parameters that contribute to the signal response of an imaging system are the MTF due to the trapping levels (MTF_{trap}) in the photoconductor, and the MTF results from the initial primary electron interaction (MTF_{pe}). Thus, the net MTF of imaging system is the product of individual MTF that is calculated due to individual effects.

$$MTF = MTF_{pe} \times MTF_k \times MTF_{ap} \times MTF_{ap} \qquad 2.2)$$

The MTF of an imaging system rolls down to zero at a spatial frequency (f) known as the Nyquist frequency. This frequency is determined by pixel pitch (a) in the imaging detectors and the Nyquist frequency can be expressed as $f_{ny} = 1/(2a)$. For the spatial frequencies above Nyquist, the quality of the image formed will be distorted due to aliasing. Hence the aperture MTF invariantly determines the ability of the detector for imaging under different spatial frequencies.

The expected MTF behavior of any practical imaging detector can be associated with the aperture MTF as shown in Figure 2.6.

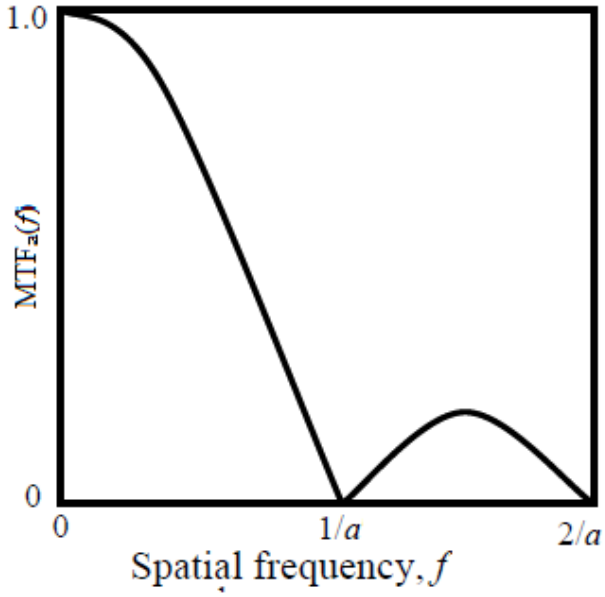

Figure 2.6: Aperture MTF, expected MTF in any practically used imagers (Here a is the size of the pixel) [21]

2.2.6 Detective Quantum Efficiency

The imaging ability of any imaging system has been qualified with Detective Quantum Efficiency (DQE). It defines the ability of the imaging system to transfer the signal with different spatial frequencies from input to output with the minimal addition of noise. Hence DQE can be conveniently defined as the ratio of SNRs at the output to input.

$$DQE(f') = \frac{SNR_{out}^2(f)}{SNR_{in}^2(f)} \tag{2.3}$$

Ideally, an imaging system will possess a DQE equals unity. But in practice due to various physical phenomena, the DQE rolls off from the ideal case. One primary reason is due to severe variation in the spatial frequency of the object that must be imaged. Moreover, the deep trapped charges and reabsorption of K-fluorescence lay down the law for DQE roll-off. The deeply trapped charges in the semiconductor create a non-uniform charge collection and this, in turn, adds additional noise in the system. Hence the DQE of the system starts to deviate from unity. Moving

on, the DQE reduction due to K-fluorescence reabsorption constitutes an important mechanism. When X-rays strikes the photoconductor, it releases numerous primary electron but some electrons, which corresponds to the K-edge energy, are reabsorbed and includes an undesired noise during the imaging process. This mechanism is prone when photoconductor which has a K-edge energy in the range of diagnostic medical imaging are used. Naturally a frequency dependent DQE is preferred to explain the performance of the system. But for convenience and to avoid the complexity of calculations the DQE at spatial frequency zero $(f = 0)$ is chosen. DQE at zero spatial frequency $(DQE(0))$ signifies the decrease in the DQE performance of the imaging system without considering the signal spread.

DQE has a dependency with MTF of the system. The MTF can be defined as the image blur that is caused due to the scattering of image quanta. The relation between the DQE and MTF of the system can be expressed as,

$$DQE(f) = \frac{DQE(0)MTF^2(f)}{NPS(f)} \tag{2.4}$$

Where, $NPS(f')$ is the noise power spectrum which can be approximated to one as spatial frequency tends to zero.

2.2.7 Ghosting

Ghosting is defined as the change in X-ray sensitivity of the photoconductor due to the previous exposure of radiations. Consider the Figure 2.7, where the X-rays are projected on a small rectangle (left figure) then the X-rays are projected on the entire area. It becomes evident that it forms a shadow image in the subsequent exposure. Thus, the ghosting reduces the pixel sensitivity as well as it also worsens the image quality that has been formed. This phenomenon becomes a significant threat when imaging is done in subsequent rapid frames (e.g.) fluoroscopy.

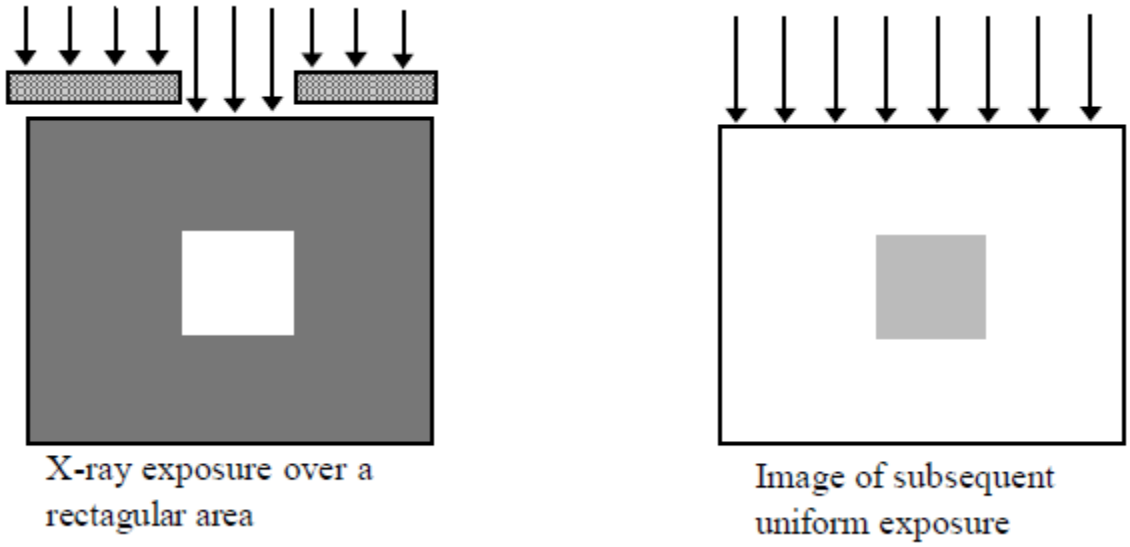

Figure 2.7: Ghosting (change in X-ray sensitivity due to previous uniform exposure) of a photodetector

2.3 Properties of an ideal X-ray Photodetector

The essential properties that an ideal X-ray photodetector should pose when used in medical imaging are as follows [22],

1. An ideal X-ray photodetector must have high quantum efficiency (η), this condition is achievable when the penetration depth (δ) of incident X-ray does not exceed the thickness *(L)* of the detectors $(\delta < L)$. That means, it should have a higher attenuation coefficient.
2. The electron-hole pair creation energy $(W_{\pm})$ must be low in order to create a sufficient number of collectible electron-hole pairs per unit incident radiation.
3. Recombination in the bulk of photodetectors should be negligible.
4. Schubweg length, the mean distance a carrier travels by drifting before it becomes unavailable for conduction, for both the holes and electron should be greater than the thickness of the detector $(\mu\tau F > L)$. This condition improves the charge transport property of the photoconductor.
5. The most challenging condition that should be fulfilled by an imaging detector is to pose extremely low dark current. An ideal X-ray imaging detector will hold zero dark current under no illumination of X-rays. But in practice, the most acceptable level of dark current is in the

range of 10-1000 pA/cm^2. These very low values of the dark currents are achievable by careful engineering of a device structure to prevent any injection of carriers from the contacts.

6. Imaging detectors must be able to easily deposit uniformly over the entire Active Matrix Array (AMA). Although excellent charge transport properties are achievable in many single crystal imaging detectors, this condition prevents their commercialization as single crystal has the constraint over large area deposition. Hence a better choice is the utilization of polycrystalline or amorphous materials in X-ray imaging.
7. X-ray fatigue, deterioration of photodetector properties by repeated exposure to X-ray radiation, should be negligible.

Perovskite materials ($CH_3NH_3PbI_3$ and $CH_3NH_3PbBr_3$) in this research work have been critically evaluated by accounting most of the above-mentioned criteria for X-ray imaging.

2.4 Summary

Thus, in this chapter, the structural and electronics properties of different perovskite materials are explained and compared with each other. Furthermore, the basic parameters used in understanding an X-ray imaging detectors are briefed. Towards the conclusion, the qualificative constraints for an X-ray imaging system are highlighted.

Chapter 3: Analytical evaluation of organic perovskites

The imaging performances of perovskite photoconductors are evaluated in this chapter. This work has already been published [1].

3.1 Abstract

Enhancing the sensitivity of a direct conversion flat panel X-ray imaging detector with minimum manufacturing cost has been a major dream for long decades. This criterion has been recently addressed by the usage of $MAPbX_3$ (MA is CH_3NH_3 and X is a halogen atom such as Cl, I, or Br) perovskite in X-ray imaging detectors. Though $MAPbI_3$ has shown large area deposition capability and good X-ray sensitivity, it has to fulfill other criteria such as low dark current, high spatial resolution and high signal to noise transfer capabilities. This paper evaluates the imaging performances such as X-ray sensitivity, detective quantum efficiency (DQE) and modulation transfer function (MTF) of organic perovskites (e.g., $MAPbI_3$ and $MAPbBr_3$) with a comparison to amorphous selenium (a-Se). These perovskite materials have slightly higher linear attenuation coefficients than a-Se and the expected X-ray sensitivity of these two perovskite photoconductors is higher than a-Se. The mechanisms of the dark current and photocurrent gain in the $MAPbI_3$ detector are also investigated. The $MAPbI_3$ detector shows some photocurrent gain, which is due to the enhanced electron injection under X-ray illumination. The expected theoretical zero spatial frequency DQE of the $MAPbI_3$ detectors is similar to that of a-Se while the $MAPbBr_3$ detector establishes a better DQE than a-Se. The expected MTF of the $MAPbBr_3$ detectors is similar to that of a-Se while the $MAPbI_3$ shows worse resolution than a-Se. Based upon our theoretical investigation, we believe that the organic perovskite can find its state of the art in near future if rigorous research for improving the charge carrier transport properties and optimizing its detector structure for low dark current were to be made.

3.2 Introduction

Mounting the image of the internal organs with minimal dose rate on the patient has been one of the greatest challenges faced by recent medical imaging techniques. Amorphous selenium (a-Se) is the most successful photoconductor for the direct conversion (the incident X-rays directly

[1] **D. M. Panneerselvam** and M. Z. Kabir, "Evaluation of organic perovskite photoconductors for direct conversion X-ray imaging detectors", *Journal of Materials Science: Materials in Electronics*, **vol. 28**, no. 10, pp. 7083-7090, 2017.

generate electron and hole pairs, EHPs, in the photoconductor layer) flat-panel digital X-ray detectors because of its low dark current, convenient deposition over large area, good charge carrier transport properties (mobility and lifetime) and moderate X-ray sensitivity [23, 24, 25]. Recently, Yakunin et al. [26] reported that a thick layer (~100 μm) of polycrystalline methylammonium lead iodide (poly-$MAPbI_3$ where MA is CH_3NH_3) perovskite can be uniformly deposited over a large area using a solution based synthesis technique without affecting the underline Active Matrix Array (AMA) electronics. This material also shows a reasonable X-ray absorption coefficient and its X-ray sensitivity is comparable to a-Se. Therefore, $MAPbI_3$ can be a potential candidate for large area X-ray detectors that leads to a new class of perovskite large-area X-ray sensors. Although the reported 60 μm thick detector [26] shows a reasonable level of photocurrent for the X-ray fluence of 1.4×10^7 photons mm^{-2} s^{-1}, the dark current is almost half of the photocurrent, which is not desirable for X-ray imaging. Moreover, the detectors show some photocurrent gain, which will have some effects on the imaging performances. Therefore, it is vital to investigate the origin of the photocurrent gain and high dark current and analyze the detector performances by physics-based theoretical models.

In this paper, we examine the effects of X-ray interaction and charge transport properties on the imaging performances such as X-ray sensitivity, detective quantum efficiency (DQE) and modulation transfer function (MTF) of organic perovskites (e.g., $MAPbI_3$ and $MAPbBr_3$ [27]). We also analyze the photocurrent characteristics with our physics-based theoretical model [28, 29] and compare the theoretical results with the experimental data. We evaluate the quantity of signal that could be lost due to traps or any recombination centers in the $MAPbI_3$ and hence determine the actual photocurrent gain. The mechanisms of the dark current and photocurrent gain in the $MAPbI_3$ are also studied. We find that the detector structure and the dark current mechanisms are equally important as the charge carrier transport and X-ray absorption properties.

3.3 Characteristics of perovskite photoconductors

$MAPbI_3$ is a direct bandgap semiconductor of bandgap energy of 1.6 eV and the relative dielectric constant of 28. Its density is 4.3 g/cm^3 [30]. The electron and hole mobilities in polycrystalline films are ~8 and ~15 cm^2/Vs, respectively [26]. The dark resistivity is ~ 10^9 Ωcm. The effective masses of electrons and holes are $0.23m_0$ and $0.29m_0$ respectively [31], where m_0 is the free electron mass. The bandgap of $MAPbBr_3$ is 2.3 eV [32], density is 3.8 g/cm^3 and the

relative dielectric constant is 28 [33]. The electron and hole mobilities in crystalline $MAPbBr_3$ are 190 and 206 cm^2/Vs, respectively [27].

The basic detector structure consists of a photoconductor layer that is sandwiched between two parallel plate electrodes. The top electrode (the radiation-receiving electrode) is biased with a voltage V to establish an electric field F across the photoconductor layer and the charge is collected from the bottom electrode. The biasing voltage can be positive if the holes have superior transport properties (the product of mobility μ and carrier lifetime τ) and negative for the superior transport properties of electrons.

The effects of charge transport properties and attenuation coefficient of photoconductor materials on the detector performances depend on the photoconductor thickness L and electric field F through the following normalized parameters; the normalized attenuation depth (attenuation depth/thickness) $\Delta = 1/(\alpha L)$, the normalized electron schubweg (electron schubweg per unit thickness) $x_e = \mu_e \tau_e F/L$, and the normalized hole schubweg (hole schubweg per unit thickness) $x_h = \mu_h \tau_h F/L$. Here α is the linear attenuation coefficient of the photoconductor, $\mu_{e(h)}$ is the mobility, and $\tau_{e(h)}$ is the deep trapping time (lifetime) of electrons (holes). The schubweg ($\mu\tau F$) is the distance a carrier drifts before it is deeply trapped and unavailable for conduction. The subscripts h and e stand for holes and electrons respectively. Equivalently, x_e and x_h are the normalized carrier lifetimes (carrier lifetimes per unit transit time) for electrons and holes, respectively.

3.3.1 Attenuation Coefficient

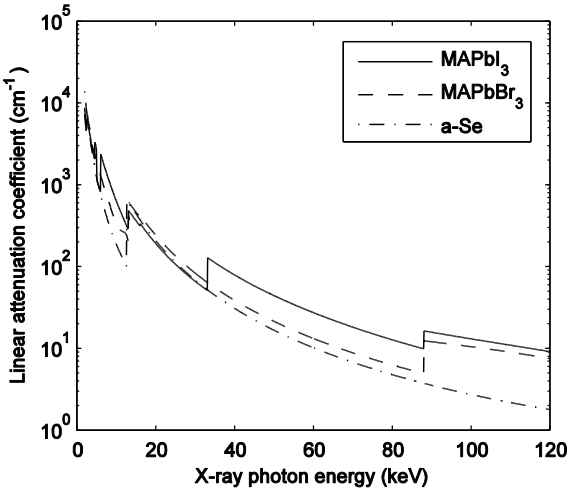

Figure 3.1: Linear attenuation coefficients of $MAPbI_3$, $MAPbBr_3$, and a-Se

The linear attenuation coefficients of $MAPbI_3$, $MAPbBr_3$, and a-Se photoconductors as a function of X-ray photon energy (E) are shown in Figure 3.1. The mass attenuation coefficient data for each element in the compound was obtained from the Nist website [34]. The mass attenuation coefficient of a compound is the weighted average (by weight using elemental atomic masses) of the elemental mass attenuation coefficients [35]. The X-ray attenuation in these compound materials is mainly controlled by the heavier elements. For example, the attenuation coefficient of $MAPbI_3$ is almost identical to PbI_3. The k-edges of lead, iodine, bromine and selenium are at 88, 33.17, 13.47 and 12.64 keV respectively. Therefore, in chest radiographic and fluoroscopic applications (average X-ray photon energy of ~53-60 keV), the blurring due to the k-fluorescence reabsorption in $MAPbI_3$ (due to iodine atom) is more pronounced than that in $MAPbBr_3$ and a-Se detectors. As evident from Figure 1, the perovskite materials have slightly higher linear attenuation coefficients than a-Se. Therefore, these materials are suitable for the direct conversion X-ray image detectors. The attenuation depths in $MAPbI_3$ at photon energies of 20 and 60 keV are 52 and 365 μm, whereas the attenuation depths in $MAPbBr_3$ are 41 and 757 μm, respectively. The photoconductor layer thickness has to be at least larger than the attenuation depth for a reasonable level of X-ray absorption. The X-ray photon energy dependent X-ray quantum efficiency $\eta(E)$ is given by,

$$\eta(E) = 1 - e^{-\alpha(E)L} \tag{3.1}$$

3.3.2 X-ray sensitivity

The X-ray sensitivity (S) of a photoconductive detector is defined as the collected charge per unit area per unit exposure of radiation and is considered an important performance measure for a superior image. High S permits the use of low detector radiation-exposure levels which also increases the dynamic range of the flat panel detectors. The selection of the X-ray photoconductor is highly influenced by the value of S.

The value of S can be considered to arise in terms of three controlling factors: firstly, the amount of radiation actually absorbed from the incident radiation that is useful for the generation of electron–hole pairs (EHPs), which is characterized by the quantum efficiency η; secondly, the generation of EHPs by X-ray interactions, which is characterized by the value of the electron-hole pair creation energy $W_{\pm}$ (it is the average energy required to create a single EHP) of the

photoconductor and thirdly, how much of the X-ray generated charge is actually collected in the external circuit. The later is characterized by the charge collection efficiency η_{cc}. If the top electrode is positively biased, the η_{cc} for a monoenergetic X-ray beam is given by [28]

$$\eta_{cc}(E) = x_h\left[1+\frac{1}{\eta(\Delta/x_h-1)}\left(e^{-\frac{1}{x_h}}-e^{-\frac{1}{\Delta}}\right)\right]+x_e\left[1-\frac{1}{\eta(\Delta/x_e+1)}\left(1-e^{-\frac{1}{\Delta}-\frac{1}{x_e}}\right)\right] \tag{3.2}$$

It is assumed in equation (3.2*)* that the electric field is uniform across the photoconductor layer under small signal operation, which is the case in diagnostic X-ray detectors [36]. If the bias polarity is reversed, then x_e and x_h must be interchanged in equation (3.2*)*. The X-ray Sensitivity S of an X-ray imaging detector is conveniently normalized with respect to the maximum sensitivity (S_0) that would arise if all the incident radiation were absorbed and all the liberated carriers were collected. The charge collection and absorption-limited normalized sensitivity s for a monoenergetic X-ray beam is,

$$s(E) = S/S_0 = \eta(E)\eta_{cc}(E) \tag{3.3}$$

Assuming a sufficiently thick photoconductor layer so that the fluorescent X-rays (if any) are reabsorbed within the photoconductor layer, the expression for S_0 is given by, [37]

$$S_0(E) = \frac{5.45\times10^{13}\,e}{(\alpha_{air}/\rho_{air})W_{\pm}} \tag{3.4}$$

where e is the elementary charge, α_{air} and ρ_{air} are the energy absorption coefficient of air and its density. If $W_{\pm}$ is expressed in eV, α_{air}/ρ_{air} is in $cm^2\ g^{-1}$ and exposure (symbol not in equation (3.4*)*) is in Roentgens, then S_0 is in $Ccm^{-2}\ R^{-1}$.

Figure 3.2 shows the X-ray sensitivity of (a) $MAPbI_3$ and (b) $MAPbBr_3$ photoconductors as a function of photoconductor thickness at different electric fields and for mammographic applications (The X-ray photon energy, E = 20 keV). The values of $W_{\pm}$ in $MAPbI_3$ and $MAPbBr_3$ are taken as 5 and 6 eV as used in Refs. [26] & [27]. We believe that these are approximately the theoretical values according to the Klein rule, $2.8E_g + E_{phonon}$ [38], where E_{phonon} is the phonon energy. With E_g ~1.6 eV and E_{phonon} < 0.5 eV, we would expect that $W_{\pm}$ ~5 eV. As mentioned in section 3.3.1, since the attenuation coefficient of $MAPbI_3$ is almost identical to PbI_3 one would expect that the value of $W_{\pm}$ in $MAPbI_3$ should be almost the same as in PbI_3 (in fact, $W_{\pm}$ ~ 5 eV in

PbI_2 [39]). Note that there is no experimentally reported values for $W_{\pm}$ in literature for these two perovskites. The mobility of electrons and holes are 6 and 19 cm^2/Vs for $MAPbI_3$ [26] whereas these are 190 and 206 cm^2/Vs in $MAPbBr_3$ [27]. The lifetimes of electrons and holes are 100 and 42 ns in $MAPbI_3$ [26], and 150 and 70 μs in $MAPbBr_3$ [27]. Considering the same transport parameters mentioned above, the X-ray sensitivities of (a) $MAPbI_3$ and (b) $MAPbBr_3$ photoconductors as a function of photoconductor thickness for chest radiographic applications (E = 60 keV) are shown in Figure 3.3. There exists an optimum thickness to achieve maximum sensitivity and the optimum thickness increases with increasing electric field and photon energy. Furthermore, while maintaining much higher X-ray sensitivity, the required electric field is very low (below 20 V/cm) across the single crystal $MAPbBr_3$ photoconductor, because of its excellent charge transport properties (the mobility-lifetime products in $MAPbBr_3$ are three orders of magnitude higher than that in polycrystalline $MAPbI_3$). Note that the electric field beyond 20 V/cm is not required for the maximum sensitivity in $MAPbBr_3$ whereas one can expect even higher sensitivity by increasing the field beyond 2 V/μm in $MAPbI_3$. However, the electric field above 2 V/μm is not practical because the dark current might be very high at this high field. The typical values of X-ray sensitivity of a-Se mammographic and chest radiographic detectors are 0.25 and 3-4 $\mu Ccm^{-2}\ R^{-1}$, respectively [39]. The expected X-ray sensitivity of these two perovskite photoconductors is higher than a-Se. Although the sensitivity of crystalline $MAPbBr_3$ is excellent, it may not be suitable for a large area X-ray detectors for diagnostic application because of its constraint on large area deposition.

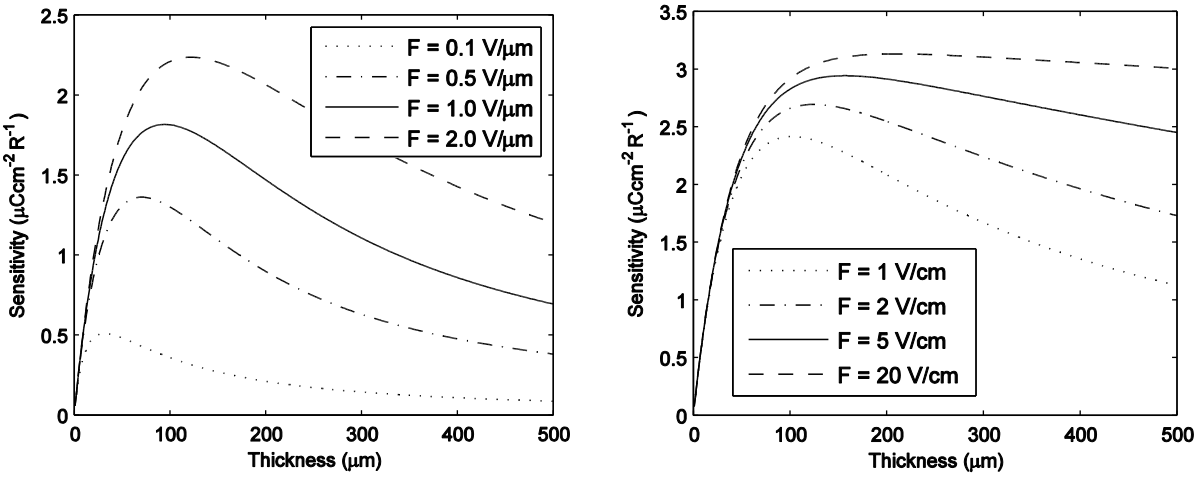

(a) (b)

Figure 3.2 Sensitivity versus thickness at different electric fields in (a) $MAPbI_3$ and (b) $MAPbBr_3$ detectors for mammographic applications (E = 20 keV).

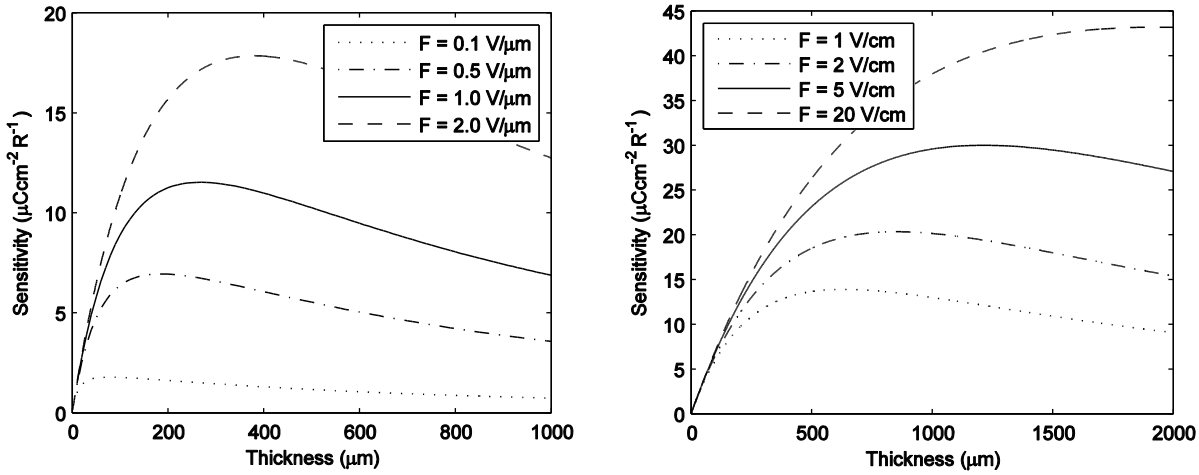

(a) (b)

Figure 3.3 Sensitivity versus thickness at different electric fields in (a) $MAPbI_3$ and (b) $MAPbBr_3$ detectors for chest radiographic applications (E = 60 KeV).

3.3.3 X-ray Photocurrent

The duration of the X-ray exposure is usually much higher than the fastest carrier transit time. The photocurrent due to an individual carrier transport (electron or hole) reaches almost a steady value after its transit time. The photocurrent density due to hole transport under positive bias is given by [29],

$$J_h(t)=\begin{cases}\dfrac{Ae\mu_h F}{\alpha L}\{[1-\exp(-t/\tau_h)(1-\alpha\mu_h\tau_h F)-\exp(-\alpha L)[1-\exp(-t/\tau_h+\alpha\mu_h Ft)]\};0<t<T_h \\ \dfrac{Ae\mu_h F}{\alpha L}\{[1-\exp(-\alpha L)]-\alpha\mu_h\tau_h F[1-\exp(-L/\mu_h\tau_h F)]\};t>T_h\end{cases} \quad (3.5)$$

where $A=\dfrac{G_0\tau_h}{1-\alpha\mu_h\tau_h F}$. The expression of G_0 (in $cm^{-3}s^{-1}$) is given by [29],

$$G_0(E)=\frac{5.45\times10^{13}\,\alpha X}{(\alpha_{air}/\rho_{air})W_{\pm}T_{ex}} \quad (3.6)$$

where t is the instantaneous time, T_{ex} is the exposure time and X is the amount of exposure/dose. If $W_{\pm}$ is expressed in eV, α_{air}/ρ_{air} is in $cm^2\ g^{-1}$, α is in cm^{-1}, X is in Roentgens and T_{ex} in seconds, then G_0 is in $cm^{-3}\ s^{-1}$.

Similarly, the photocurrent density due to electron transport is [29],

$$J_e(t)=\begin{cases}\dfrac{Be\mu_e F}{\alpha L}\{[1-\exp(-t/\tau_e-\alpha\mu_e Ft)]-(1+\alpha\mu_e\tau_e F)\exp(-\alpha L)[1-\exp(-t/\tau_e)]\};0<t<T_e \\ \dfrac{Be\mu_e F}{\alpha L}\{[1-\exp(-\alpha L)]-\alpha\mu_e\tau_e F\exp(-\alpha L)[1-\exp(-L/\mu_e\tau_e F)]\};t>T_e\end{cases} \quad (3.7)$$

Where $B=\dfrac{G_0\tau_e}{1+\alpha\mu_e\tau_e F}$.

The total photocurrent density, $J_{ph}=J_h+J_e$.

Figure 3.4 shows the current as a function of electric field in a $MAPbI_3$ detector. The symbols represent the experimental data, which are extracted from Ref. [26]. The dark conductivity of this material is $\sigma\sim1.4\times10^{-9}$ Scm^{-1}. Considering the contacts are ohmic-type, the dark current (the current density = σF) becomes almost three times larger than the measured values. Therefore, the current is probably limited by the Schottky emission from the metal contacts. The electron injection is more probable than the hole injection as discussed by Dong et al. [40]. The electron injection current density can be written as [24],

$$J_{inj}=eN_C\mu_e F\exp\left(-\frac{\phi_e}{kT}\right) \quad (3.8)$$

where N_C is the effective density of states in the conduction band, ϕ_e is the effective barrier height for the electron injection, k is the Boltzmann constant and T is the absolute temperature. The dashed, dash-dotted and solid lines in Figure 3.4 represent the fitting of equation (3.8*)* with experimental results under no illumination, the theoretical photocurrent and the model fit to the experimental data under X-ray illumination, respectively. The photon energy E = 8 keV and exposure rate is 2 R/s (2 mR per 1 ms), which corresponds to 1.4×10^7 photons mm^{-2} s^{-1}. The electron-hole pair creation energy, $W_{\pm}$ = 5 eV, L = 60 μm, $N_C = 2.8\times10^{18}$ cm^{-3}, μ_e = 6 cm^2/Vs, μ_h = 19 cm^2/Vs, τ_e = 100 ns, and τ_h = 42 ns. The fitted values of ϕ_e under dark and X-ray illumination are 0.57 and 0.52 eV, respectively. The difference between the dash-dotted line (theoretical photocurrent) and the solid line represent the photocurrent gain, which is due to the enhanced electron injection under X-ray illumination. We believe that the enhanced carrier injection occurs due to the lack of appropriate blocking layers for the carrier injections from the metal electrodes. Under dark condition, the energy barrier for electron injection from ZnO/Ag contact is larger. The photogenerated holes are trapped near the PCBM/ZnO interface, which induces band bending, reduces the barrier thickness and thus reduces the effective barrier height (see figure 1 of Ref. [40]). The photocurrent gain is almost a linear function of the applied electric field.

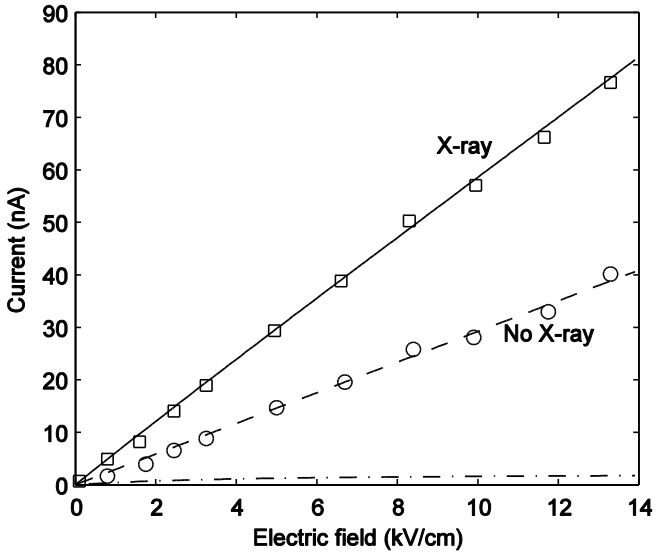

Figure 3.4 The photocurrent versus applied electric field in a $MAPbI_3$ detector. Symbols: experimental data [26], dash-dotted line: theoretical photocurrent, dashed line: model fit to the experimental dark current, and solid line: model fit to the experimental data under X-ray illumination.

The photocurrent density as a function of dose rate in a $MAPbBr_3$ detector is shown in Figure 3.5. The experimental data were extracted from Ref. [27]. The electric field, $F = 2$ V/cm, $E = 22$ keV, $W_{\pm} = 5.3$ eV, $L = 2$ mm, $\mu_e = 190$ cm^2/Vs, $\mu_h = 200$ cm^2/Vs, $\tau_e = 150$ μs, and $\tau_h = 70$ μs. The detector shows a linear behavior with the dose rate and does not show any photocurrent gain.

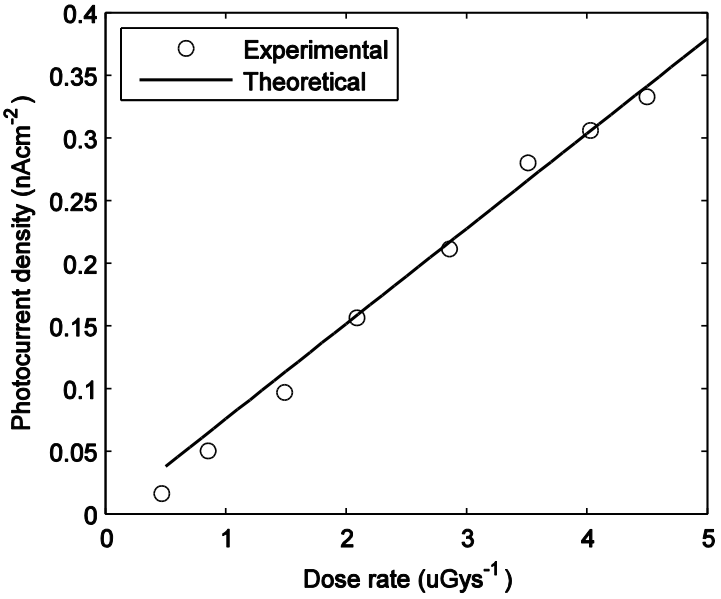

Figure 3.5: Photocurrent density versus dose rate of a $MAPbBr_3$ detector. Symbols: experimental data [27], and solid line: model fit to the experimental data under X-ray illumination.

3.3.4 Detective Quantum efficiency

The DQE measures the ability of the detector to transfer signal relative to noise from its input to its output. Images are partially degraded by various sources of statistical fluctuations that arise along the imaging chain. The relative increase in image noise due to an imaging system as a function of spatial frequency f is expressed quantitatively by DQE(f) which represents the signal-to-noise transfer efficiency for different frequencies of information in an image. The DQE(f) is defined as

$$DQE(f) = \frac{SNR_{out}^2(f)}{SNR_{in}^2(f)} \tag{3.9}$$

where SNR_{in} and SNR_{out} are the signal-to-noise ratios (SNR) at the input and output stages of the image detector, respectively. DQE(f) is unity for an ideal detector. For simplicity, we are

often interested in measuring DQE($f = 0$) of an imaging detector since it represents the signal quality degradation due to the signal and noise transfer characteristics of the system without considering signal spreading. Recently, *Kabir* et al. [41] have examined the effects of charge carrier trapping and the *K*-fluorescent X-rays on the DQE of direct conversion X-ray detectors. In this section, the DQE(0) model of *Kabir* et al. [41] is applied to a-Se, $MAPbI_3$, and $MAPbBr_3$ detectors for fluoroscopic applications to study and compare their DQE(0) performance.

Figure 3.6: DQE (0) versus exposure at different electric fields of various photoconductive detectors.shows the DQE (0) as a function of X-ray exposure for a-Se, $MAPbI_3$, and $MAPbBr_3$ detectors for a 60-keV X-ray beam. The X-ray exposure (X) is varied from 0.1 μR to 10 μR, which is the range of X-ray exposure for fluoroscopic applications. We assume that the pixel area, $A = 200\ \mu m \times 200\ \mu m$, and the effective fill factor is 1.0 for all types of photoconductors. The average E is 60 keV and the additive electronic noise (N_e) is assumed to be 2000 electrons per pixel [42]. The following transport and operating parameters are used: for a-Se detectors, $L = 1000\ \mu m$, $F = 10\ V/\mu m$, $W_{\pm} \approx 45$ eV, $\mu_e\tau_e = 10^{-6}\ cm^2/V$ and $\mu_h\tau_h = 10^{-5}\ cm^2/V$; for $MAPbI_3$ detectors, $L = 375\ \mu m$, $W_{\pm} = 5$ eV, $\mu_e\tau_e = 6\times10^{-7}\ cm^2/V$ and $\mu_h\tau_h = 8\times10^{-7}\ cm^2/V$; and for $MAPbBr_3$ detectors, $L = 680\ \mu m$, $W_{\pm} = 6$ eV, $\mu_e\tau_e = 28.4\times10^{-3}\ cm^2/V$ and $\mu_h\tau_h = 14\times10^{-3}\ cm^2/V$. The radiation-receiving electrode is biased positively for all detectors. $\Delta \approx 0.67$ is for all detectors. $\eta = 1 - \exp(-1/\Delta) \approx 0.77$ is the maximum achievable DQE(0) if all the liberated charges are collected. The DQE(0) of the $MAPbI_3$ detectors is similar to that of a-Se while the $MAPbBr_3$ detector establishes a better DQE than a-Se.

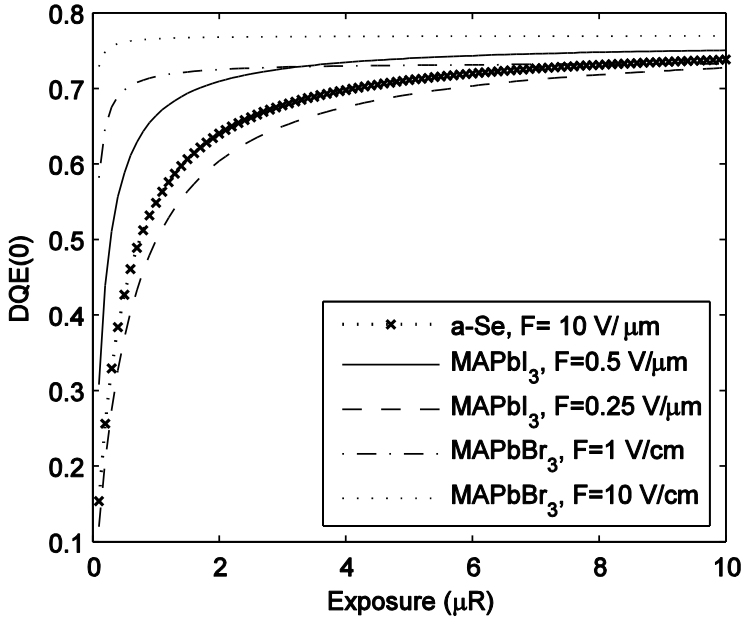

Figure 3.6: DQE (0) versus exposure at different electric fields of various photoconductive detectors.

3.3.5 Modulation transfer function

The spatial resolution of an imaging device system can be described in terms of the MTF, which is the relative response of the system as a function of spatial frequency. The MTF of an imaging system can be described as a cascade of several stages where the overall MTF is simply the product of the MTFs of all the individual stages. The overall MTF (or presampling MTF) of an image detector can be expressed as [43],

$$\mathrm{MTF}(f) = \mathrm{T}_w(f) \times \mathrm{T}_{tr}(f) \times \mathrm{T}_a(f) \tag{3.10}$$

where, $\mathrm{T}_w = p_{pe}\mathrm{T}_{pe} + p_k\mathrm{T}_k$ is the weighted MTF including the MTFs due to the range of the primary photoelectron and the k-fluorescence reabsorption [43], T_{pe} is the MTF for the range of the primary photoelectron, $\mathrm{T}_k(f)$ is the MTF due to the k-fluorescence reabsorption, $\mathrm{T}_{tr}(f)$ is the MTF due to the charge carrier trapping, $\mathrm{T}_a(f)$ is the MTF associated with the aperture function of the pixel electrodes, and p_{pe} and p_k are the relative probabilities of the released charge carriers being from the primary electron interaction and k-fluorescent X-ray reabsorption, respectively. $\mathrm{T}_a(f)$ arises due to averaging the signal over a pixel area. The aperture MTF describes how spatial frequencies are passed through the detector elements. If the aperture is square with dimension a, then,

$$T_a(f) = \left|\sin c(af)\right| = \left|\frac{\sin(\pi af)}{\pi af}\right| \tag{3.11}$$

The theoretical MTF of $MAPbI_3$ based X-ray photodetector for mammographic (E = 20 keV and L = 200 μm) and chest radiographic (E = 60 keV and L = 500 μm) applications are shown in Figure 3.7 (a) & (b). The pixel pitches for mammographic and chest radiographic detectors are 100 μm and 200 μm respectively. The analytical expressions for MTF_{pe}, $MTF_{k,}$ and MTF_{tr} are taken from [28], [41] and [44], respectively. The mobility and lifetime of carriers in Figure 7 are the same as in Figure 4 and the applied electric field F = 1 V/μm. The loss of MTF due to k-fluorescence reabsorption is absent in mammographic detectors because the average X-ray energy (20 keV) is lower than the k-edge of iodine (33.17 keV). The MTF_{tr} has a very significant effect on the overall MTF because of poor charge carrier transport properties in polycrystalline $MAPbI_3$. The overall MTF of the mammographic detector is much better than that of chest radiographic detectors. The overall MTF of mammographic detectors is mainly determined by the trapping limited MTF_{tr}. On the other hand, in chest radiographic detectors, both MTF_k and MTF_{tr} control the overall MTF. The overall MTF deviates quite significantly from the aperture MTF.

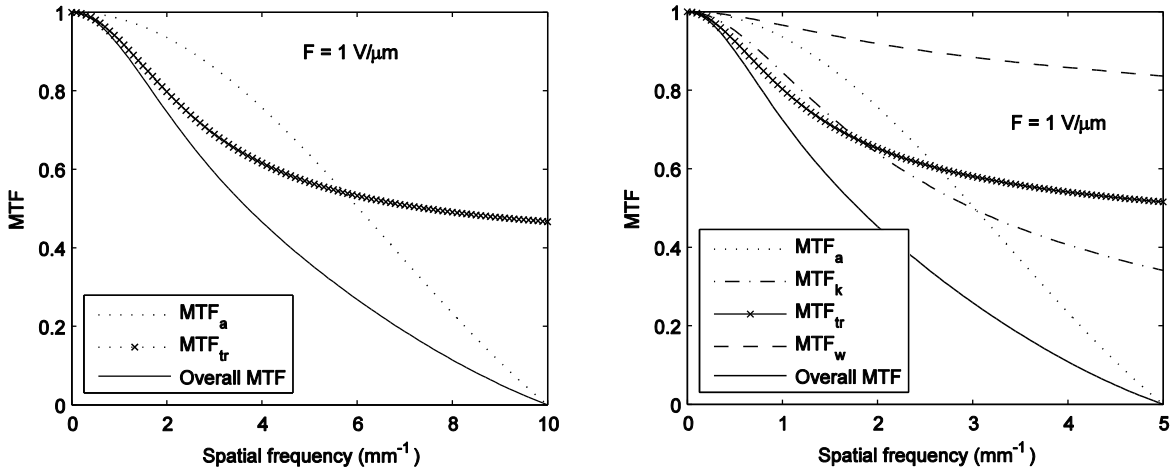

(a) (b)

Figure 3.7: The theoretical MTF of $MAPbI_3$ based X-ray photodetector for (a) mammographic (E = 20 keV and L = 200 μm) and (b) chest radiograghic (E = 60 keV and L = 500 μm) applications.

The theoretical MTF of $MAPbBr_3$ based X-ray photodetector for mammographic (E = 20 keV and L = 200 μm) and chest radiographic (E = 60 keV and L = 1000 μm) applications are shown in Figures 8 (a) & (b). The mobility and lifetime of carriers in Figure 3.8 are the same as in

Figure 3.5 and the applied electric field $F = 10$ V/cm. The overall MTF in mammographic detectors is very close to the aperture MTF because of very good charge carrier transport properties and low k-fluorescence X-ray photon energy of bromine (~12.1 keV). The overall MTF of chest radiographic detectors deviates quite significantly from the aperture MTF is mainly determined by the trapping limited MTF_{tr}.

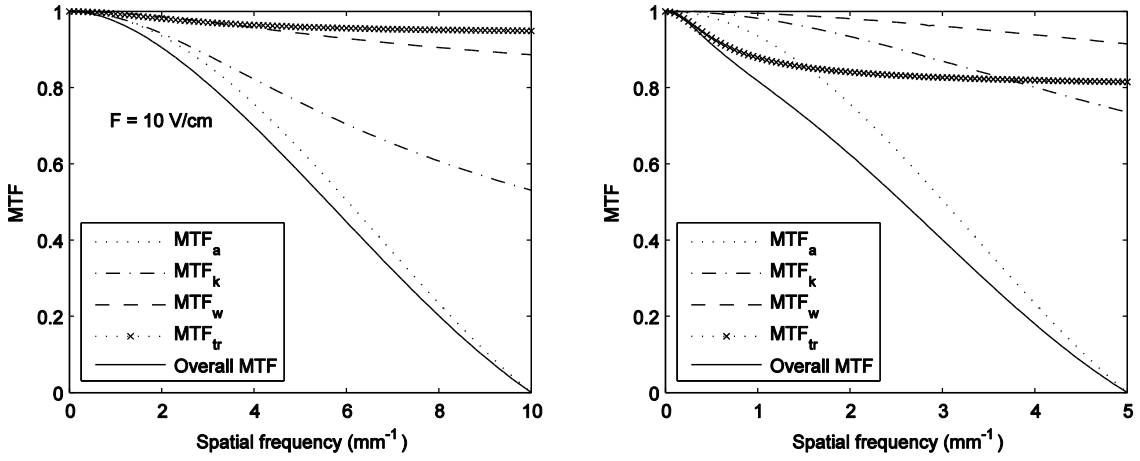

(a) (b)

Figure 3.8: The theoretical MTF of $MAPbBr^3$ based X-ray photodetector for (a) mammographic (L = 200 μm) and (b) chest radiographic (L = 1000 μm) applications

The expected resolution of $MAPbBr_3$ detectors is better than that of $MAPbI_3$ because of much better charge transport properties in $MAPbBr_3$. The expected MTF of $MAPbBr_3$ detectors is similar to that of a-Se while $MAPbI_3$ detectors show worse resolution than a-Se [45].

Thus the performance of perovskite based X- ray imaging system can be compared with the conventionally used a- Se based detector as shown in Table 3.1 [22, 26, 27, 46],

Table 3.1: Comparison of device parameters of an X-ray imaging system between different active layer [22, 26, 27, 46]

	Sensitivity ($\mu Ccm^{-2}R^{-1}$)		Detective Quantum Efficiency (DQE)	Resolution (MTF)	Dark Currents
	Mammography	Chest Radiology			
Amorphous Selenium	0.22- 0.24 (F= 10 V/μm)	2.1- 3.38 (F= 10 V/μm)	Good	Good	< 10 pA/mm^2 (F<=20 V/μm)
$MAPbI_3$ (Perovskite)	>2 (F= 2 V/μm)	>18 (F= 2 V/μm)	Good	Low	~ nA to μA
$MAPbBr_3$ (Perovskite)	>3.2 (F= 20 V/cm)	>43 (F= 20 V/cm)	Good	Good	~ nA to μA

3.4 Conclusions

The effects of X-ray interaction and charge transport properties on the imaging performances such as X-ray sensitivity, detective quantum efficiency (DQE) and modulation transfer function (MTF) of organic perovskites (e.g., $MAPbI_3$ and $MAPbBr_3$) have been analyzed. The $MAPbI_3$ detector shows photocurrent gain, which is due to the enhanced electron injection under X-ray illumination. These perovskite materials have slightly higher linear attenuation coefficients than a-Se and the expected X-ray sensitivity of these two perovskite photoconductors is higher than a-Se. The expected DQE(0) of the $MAPbI_3$ detectors is similar to that of a-Se while the $MAPbBr_3$ detector establishes a better DQE than a-Se. The theoretical MTF of the $MAPbBr_3$ detectors is similar to that of a-Se while the $MAPbI_3$ shows worse resolution than a-Se. Owing to these facts, we conclude if rigorous research were to be made for improving the charge carrier transport properties and optimizing its detector structure (e.g., appropriate metal contacts and blocking layers) for low dark current, organic perovskite has a very high potential to replace a-Se in direct conversion X-ray detectors.

Chapter 4: Numerical evaluation of organic perovskites

The analytical models described in chapter Chapter 3: are valid for small signal case (which is valid for single exposure in diagnostic medical imaging). However, under repeated exposures the accumulated trapped charges in the detector becomes significant to make the electric field profile non-uniform. In this case the analytical models are not valid and we need to develop a numerical model for performance analysis. Thus, in this chapter, numerical solution of continuity equations (solving for hole concentration p and electron concentration n) and trap rate equations (solving for trapped hole concentration p_t and trapped electron concentration n_t) were performed simultaneously using COMSOL Multiphysics. Furthermore, Poisson's equation (solving for electric potential V) was also coupled with continuity and trap equations. The sensitivity S of the perovskite materials is calculated numerically by solving ordinary differential equations (ODE) for charge density.

4.1 Equations depicting carrier transport

The continuity equation for hole and electron concentration in semiconducting materials can be defined with respect to traps and recombination terms as [29 ,47],

$$\frac{\partial p}{\partial t} = -\mu_p \frac{\partial}{\partial x}(pF) + g - \frac{p}{\tau_p} - C_r pn - C_p pn_t \tag{4.1}$$

$$\frac{\partial n}{\partial t} = \mu_n \frac{\partial}{\partial x}(nF) + g - \frac{n}{\tau_n} - C_r pn - C_n p_t n \tag{4.2}$$

where g is the carrier generation rate, F is the electric field, $\mu_{p,n}$ is the mobility of holes and electron ($cm^2V^{-1}s^{-1}$), $\tau_{p,n}$ is the lifetime of holes and electron (s), p_t and n_t are the trapped hole and electron concentration (cm^{-3}) which are derived from the trap equations as [47],

$$\frac{\partial p_t}{\partial t} = -C_p p_t n + \frac{p}{\tau_p} \tag{4.3}$$

$$\frac{\partial n_t}{\partial t} = -C_n pn_t + \frac{n}{\tau_n} \tag{4.4}$$

C_r is the bimolecular recombination coefficient between the free electrons and holes, C_p is the capture coefficient between the free electron and trapped hole and C_n is the capture coefficient between the free hole and trapped electron. The values of C_r, C_p, and C_n are calculated as [47],

$$C_r = \frac{e(\mu_p + \mu_n)}{\varepsilon}\ ,\ C_p = \frac{e\mu_p}{\varepsilon} \text{ and } C_n = \frac{e\mu_n}{\varepsilon}.$$

The generation rate of holes and electrons in $cm^{-3}s^{-1}$ can be expressed as [29, 47],

$$g = \frac{\alpha E \phi_o(E)}{T_{ex} W_{\pm}} \exp(-\alpha x) \tag{4.5}$$

where α is the linear attenuation coefficient (cm^{-1}), E is the energy of the incident photon (eV), T_{ex} is the exposure time (s), $W_{\pm}$ is the electron-hole pair creation energy (eV), and ϕ_o is the incident X-fluence (photons/cm^2), expressed as,

$$\phi_o(E) = \frac{5.45 \times 10^{13} X}{(\frac{\alpha_{air}(E)}{\rho_{air}})E} \tag{4.6}$$

where $\alpha_{air}(E)$ is the linear attenuation coefficient of air dependent on the energy of the incident photon (cm^{-1}), ρ_{air} is the density of air, and X is the exposure of incident X-ray photon (R). The instantaneous electric field $F(x, t)$, $(F = -\frac{dV}{dx})$ across the photodetector thickness is calculated dynamically using the Poisson's equation as [47],

$$-\frac{\partial^2 V}{\partial x^2} = \frac{e}{\varepsilon}(p + p_t - n - n_t) \tag{4.7}$$

From the carrier concentrations, the hole and electron current densities are calculated as [47],

$$J_h(t) = \frac{e}{L}\int_0^L \mu_p F p dx \tag{4.8}$$

$$J_e(t) = \frac{e}{L}\int_0^L \mu_n F n dx \tag{4.9}$$

The total current density (A/cm^2) is the summation of the hole and electron current densities as,

$$J = J_h(t) + J_e(t) \tag{4.10}$$

Sensitivity, S (charge collected per unit area per unit exposure) has been calculated by extracting the charge density (C) via the solution of ordinary differential equation *(ODE)* as,

$$\frac{dC}{dt} - J = 0 \tag{4.11}$$

Now the charge density is divided by the exposure X to obtain the sensitivity (S) of photoconductor as,

$$S = \frac{C}{X} \tag{4.12}$$

4.2 Results and Discussion

A positively biased photoconductor of thickness L is considered. Hence the boundary conditions $p(0,t) = 0$ and $n(L,t) = 0$ are used for solving continuity equations. $V(0,t) = V_0$ and $V(L,t) = 0$ are used as boundary conditions for solving the Poisson's equation. The initial conditions are $p(x,0) = n(x,0) = p_t(x,0) = n_t(x,0) = 0$ [47]. Using the above-mentioned boundary and initial conditions the continuity, trap and Poisson's equations are solved simultaneously using COMSOL Multiphysics 5.2a. The charge transport properties are maintained as discussed as in section 3.3.

4.2.1 Numerical evaluation of perovskite based X-ray photodetector – Mammography [26]

For an X-ray incident photon energy of 8 keV on a perovskite photoconductor ($CH_3NH_3PbI_3$) with thickness (L) of 60 μm at $F_0(=V_0/L)$= 10 kV/cm the carrier distribution across the thickness of the photoconductor is shown in Figure 4.1 and Figure 4.2. In this section 4.2.1, an exposure level of 2 mR is maintained throughout the entire exposure time of 1 ms which corresponds to 1.4×10^7 photons/mm^2/s.

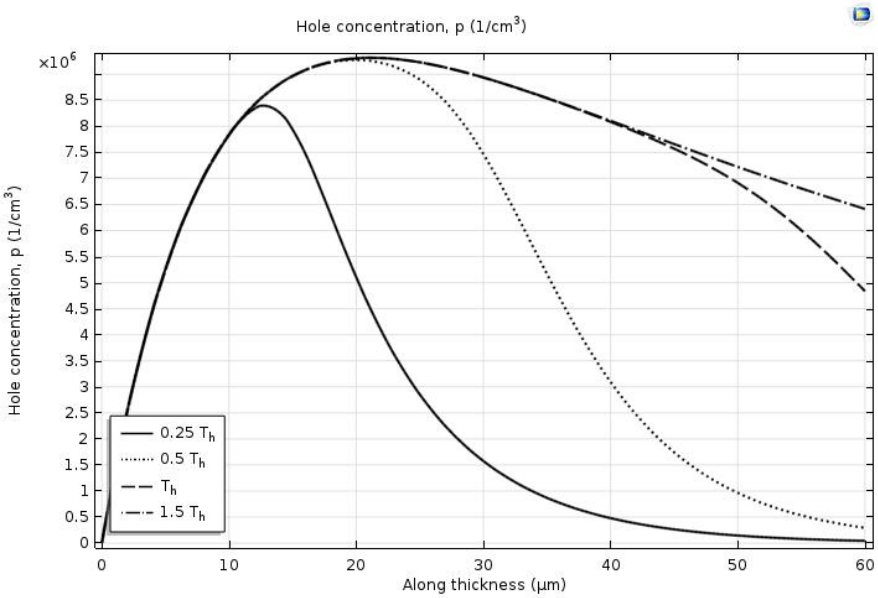

Figure 4.1: Hole concentration profile along the thickness (L= 60 µm) of photoconductor with average field, F_0= 10 kV/cm

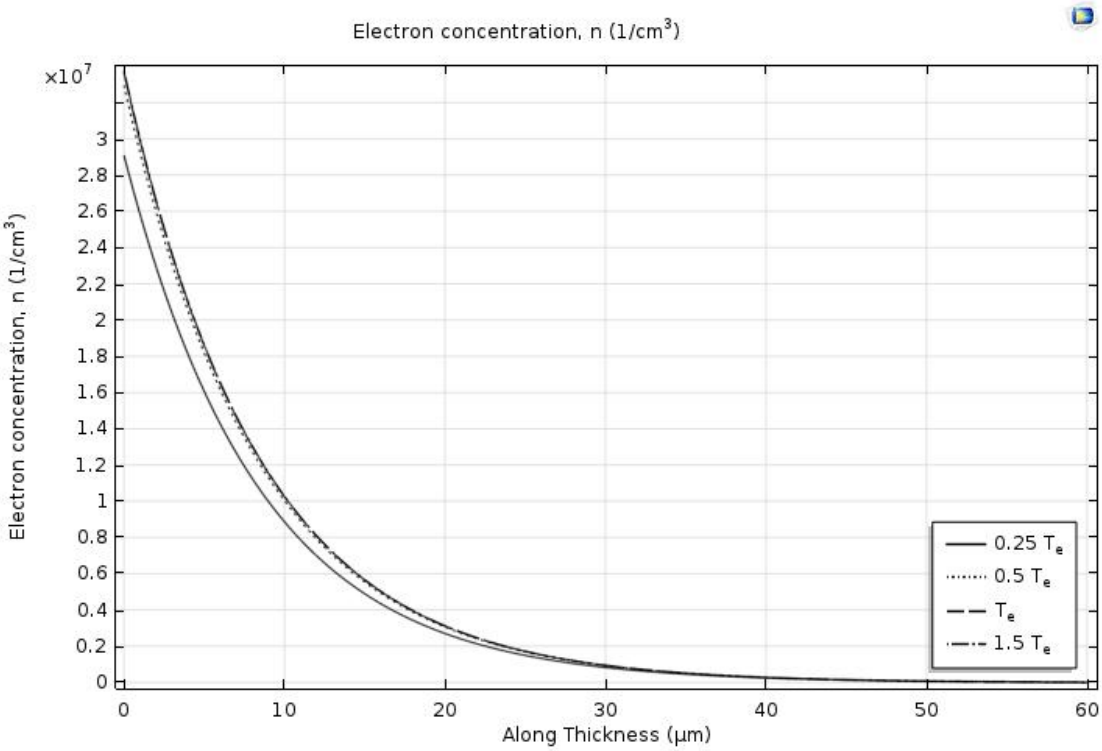

Figure 4.2: Electron concentration profile along the thickness (L=60µm) for photoconductor with average field, F_0= 10 kV/cm

The simulations for charge carrier distributions, in Figure 4.1 and Figure 4.2, are carried out for various transit times $T_{h,e}$ calculated through,

$$T_{h,e} = \frac{L}{\mu_{h,e} F_0} \tag{4.13}$$

The electron mostly resides near the top electrode because of exponential absorption and carrier generation profile. It becomes evident that the steady state values are reached just after the carrier transit times. The peak concentration of electron is higher compared with the hole concentration because of the longer lifetime of an electron in perovskite polycrystalline films. The calculated steady state current density for hole transport is 2.3197 nA/mm^2 and for electron transport is 0.45007 nA/mm^2. Since the carrier generation profile is exponential, the generated electrons quickly reach to the top electrode when the hole travel all the way down towards the bottom electrode. As a result, the hole transport mostly contributes the photocurrent.

During these calculations, the MUMPS solver in COMSOL is optimized with a damping factor of 1.45 and tolerance factor of 2.5 to avoid the stiffness during the numerical solution of partial differential equations. The meshing levels are maintained at "Finer" (Maximum element size of 0.12 μm) in user-defined semiconductor calibrations.

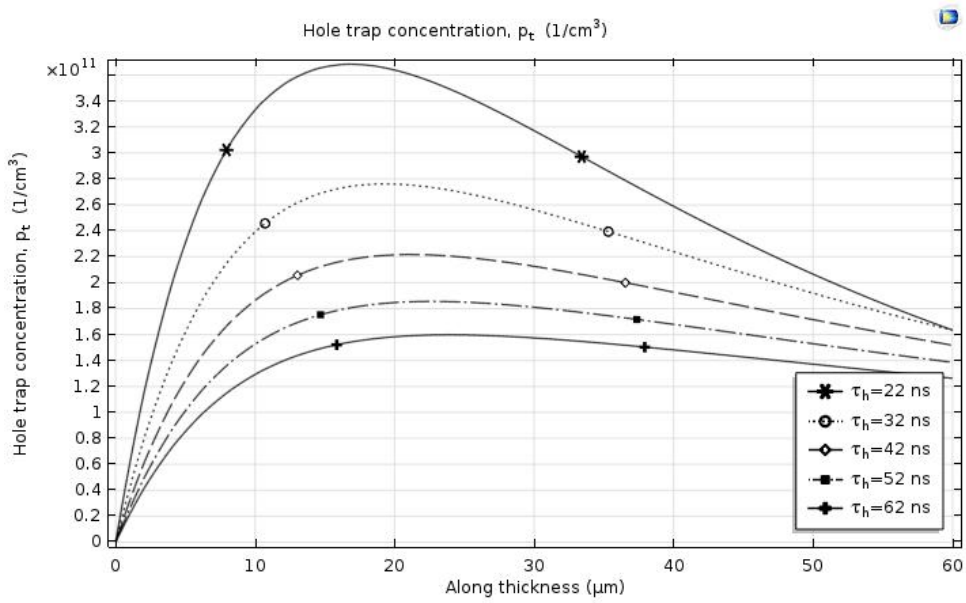

Figure 4.3: Distribution of trapped hole concentration across the thickness (L=60μm) of photoconductor at the end of exposure time with average field, F_0= 10 kV/cm

The trapped hole and electron (p_t and n_t) concentration for various lifetimes of electron and holes, at the end of exposure (T_{ex}), are shown in Figure 4.3 and Figure 4.4. From the distribution profiles of trapped electron and hole, the peak electron trap concentration is slightly higher than the hole trap concentration. However, electrons are mostly trapped near the top contact whereas holes are trapped almost all over the detector thickness.

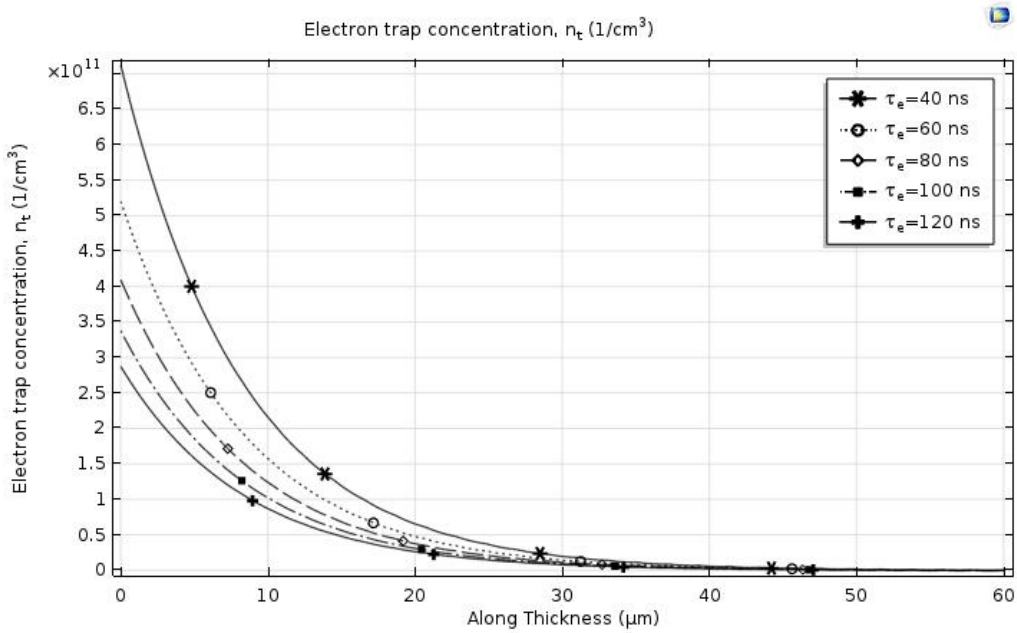

Figure 4.4: Distribution of trapped electron concentration across the thickness (L=60μm) of photoconductor at the end of exposure time with initial field, F_0= 10 kV/cm

With the obtained charge carrier distribution profiles, the photocurrent density (J) is calculated using equations (4.8), (4.9), and (4.10). From Figure 4.5, the contribution of the hole current density (J_h) to the total photocurrent density (J) is significant because of superior hole mobility (μh= 19 cm^2/V/s) in polycrystalline perovskite films. The photocurrent reaches a steady state value after carrier transit time. The steady state photocurrent calculated by this method corresponds to 2.76977 nA/mm^2.

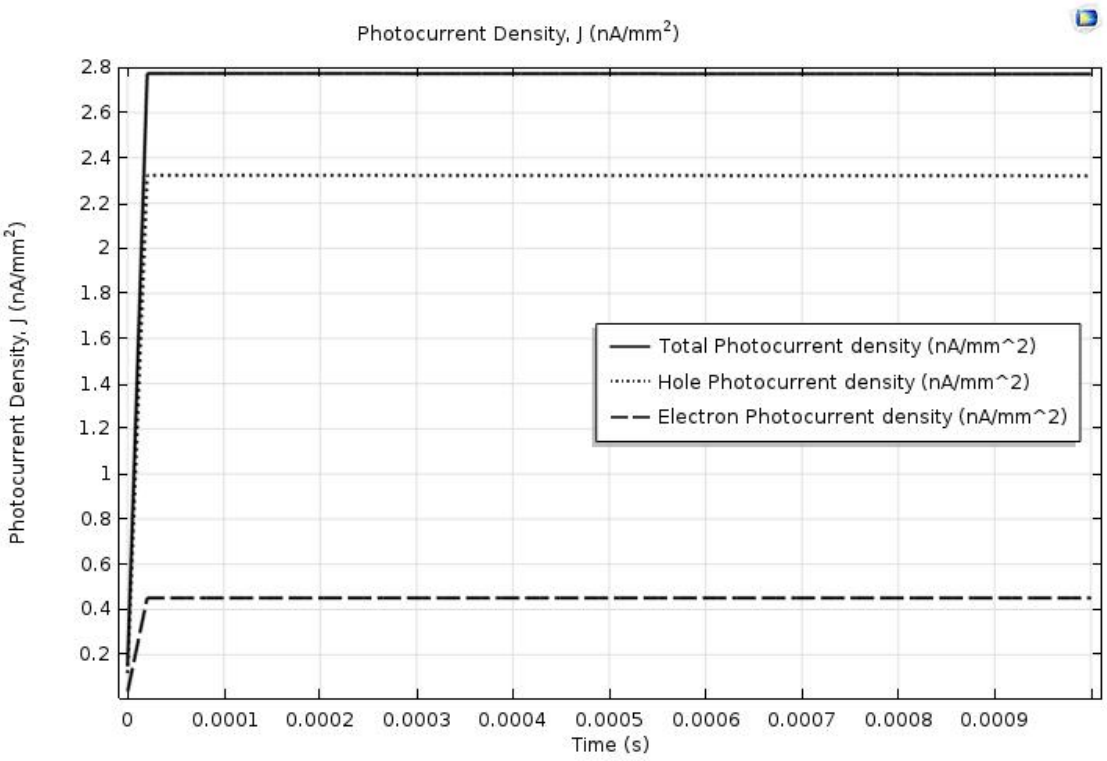

Figure 4.5: Photocurrent density vs time for *L=60μm* with average electric field, F_0= 10 kV/cm

Photocurrent density calculations are performed for the entire exposure time (T_{ex}=1 ms) with 50 time-steps (data points) from 0 to T_{ex}. Hence the meshing is reconfigured to "Coarse" (Maximum element size =1.68 μm) in user-defined semiconductor calibrations to avoid the stiffness of equations during each time sweep. Moreover, the variation of steady state photocurrent (at the end of exposure time) with respect to the electric field is shown in Figure 4.6. The photocurrent increases sub linearly with increasing electric field.

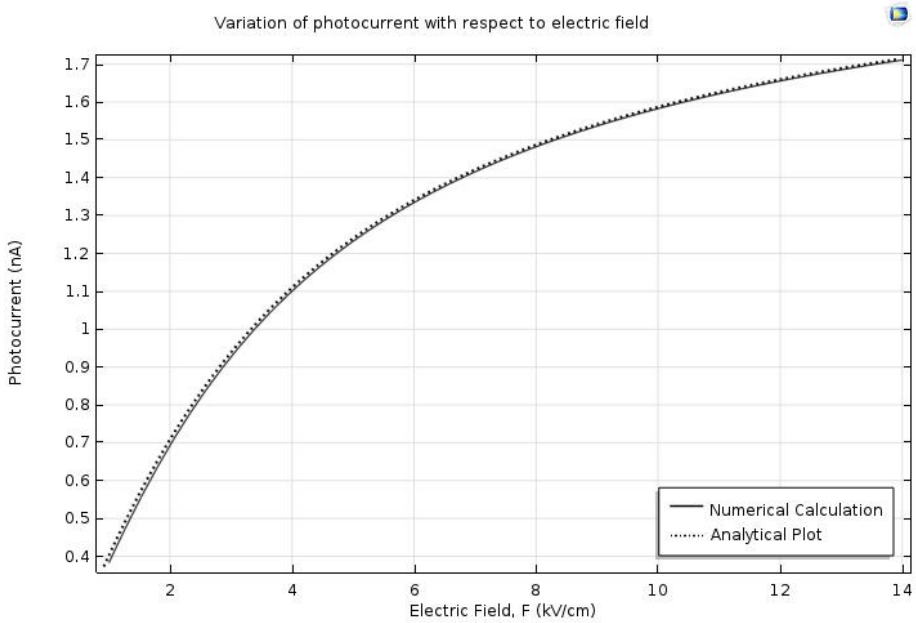

Figure 4.6: Variation of photocurrent with respect to electric Field (E= 8 keV, L=60 µm)

The electric field profile across the thickness of detector (L=60µm) for various exposure levels, at the end of exposure time (T_{ex} =1ms), considering an initial field of 10 kV/cm is shown in Figure 4.7. The fluctuation in the electric field from the initial value is significant when the exposure level increases.

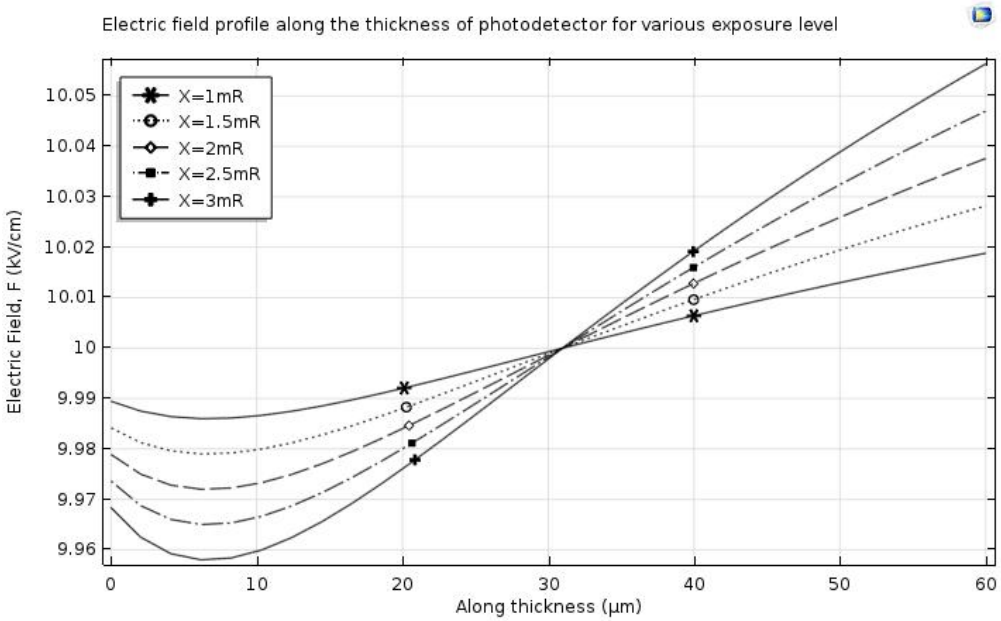

Figure 4.7: Electric Field profile across the thickness of the detector for various exposure levels at the end of exposure time (E= 8 keV, F_0= 10 kV/cm)

4.2.2 Numerical evaluation of perovskite based X-ray photodetectors – Chest Radiography

In Chest radiography, X-rays are incident with an energy of 60 keV. The average exposure level of 300 μR is maintained. The thickness of the perovskite detector (L) is optimized to 500 μm over the conventionally used 1000 μm in a-Se based X-ray photodetectors. This optimization is valid as it preserves the normalized attenuation depth ($\Delta = 1/\alpha L$) in perovskite detector over the conventionally used a-Se X-ray detector.

The charge distributions across the thickness of photodetector are shown in Figure 4.8 and Figure 4.9. From these figures, we can conclude that because of higher life time of electron, the electron concentration is higher than hole concentration. The steady state value of hole current density is 17.019 nA/mm^2 and electron current density is 11.640 nA/mm^2. The photocurrents due to hole and electron transports are comparable because of nearly uniform carrier generation at chest radiography detectors (higher x-ray photon energy). It is evident from the carrier profiles that the steady state values are reached at the end of transit time for both electron and hole.

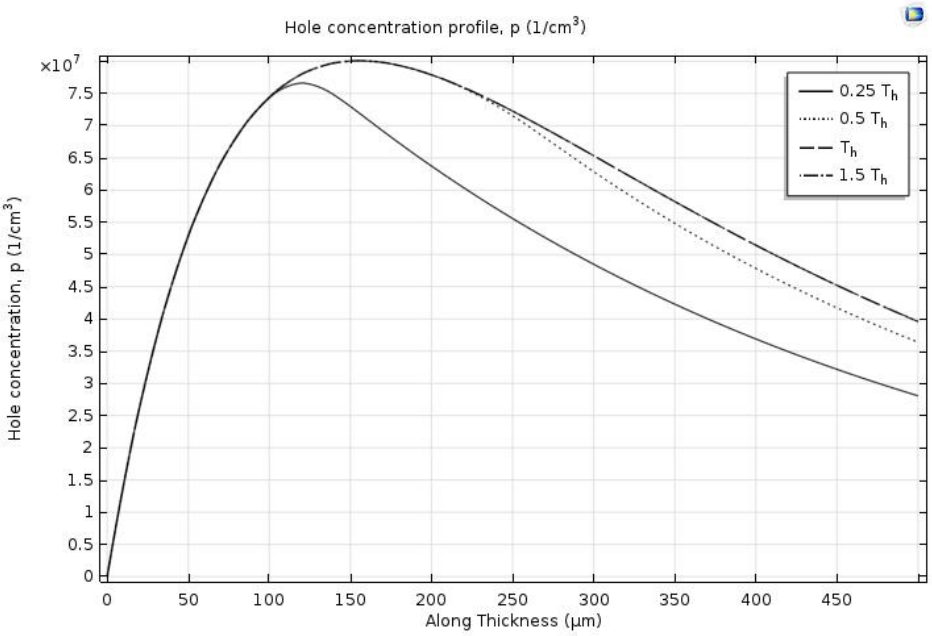

Figure 4.8: Hole concentration along the thickness of detector (L=500 μm) for chest radiography application with average field, F_0= 1 V/μm

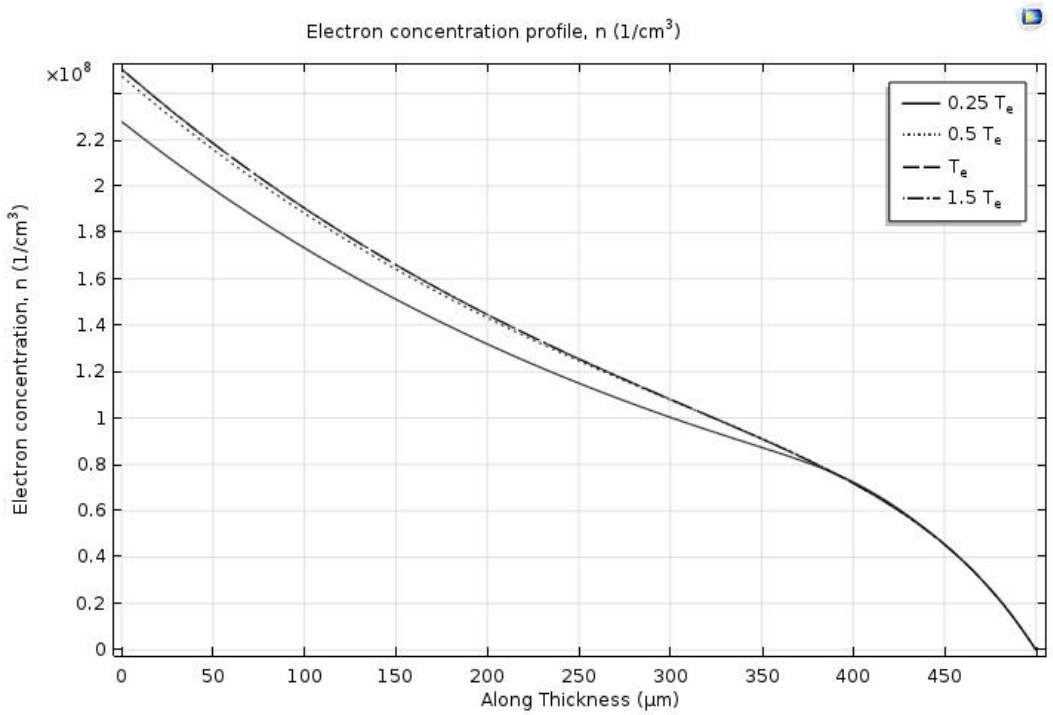

Figure 4.9: Electron concentration along the thickness of detector (L=500µm) for chest radiography application with average field, F_0= 1 V/µm

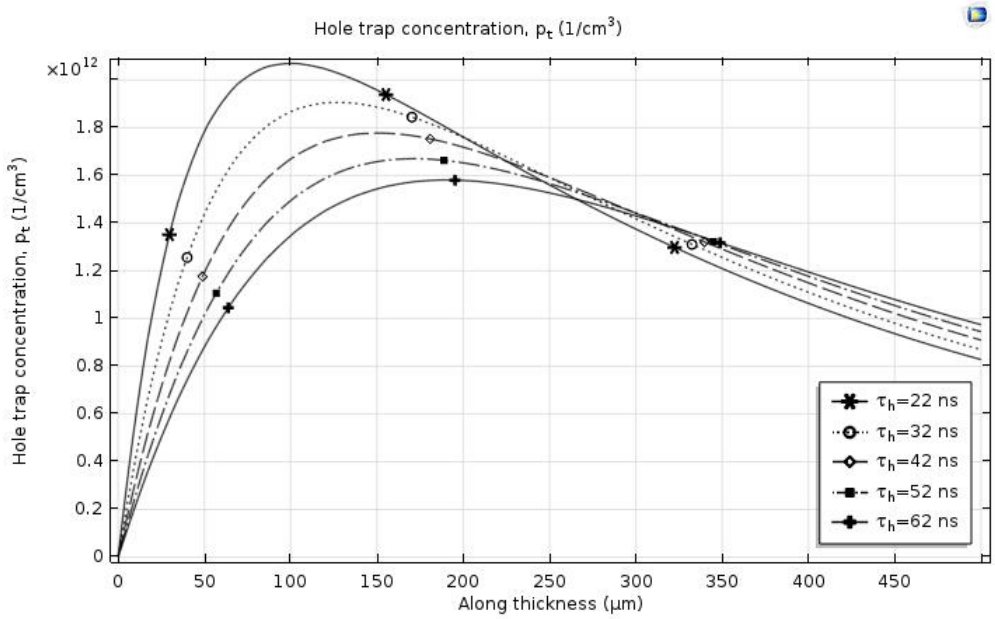

Figure 4.10: Distribution of trapped hole concentration across the thickness (L=500µm) of photoconductor at the end of exposure time with average field, F_0= 1 V/µm

Figure 4.10 and Figure 4.11 shows the trapped hole and electron concentration across the thickness of photodetector for various lifetimes of holes and electron. From these figures, the peak concentration of trapped electrons is greater than the concentration of trapped holes. And the trapped carrier concentration increases with a decrease in lifetime of carriers.

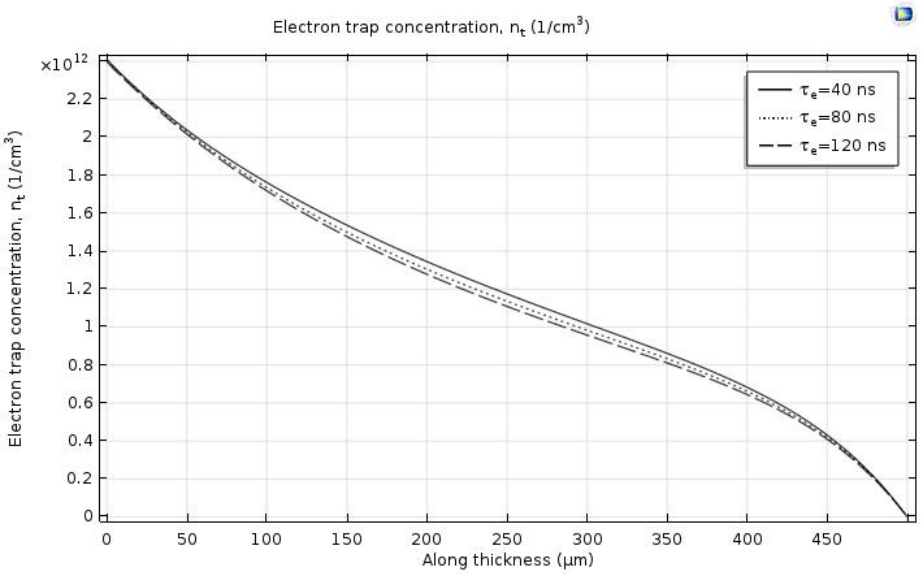

Figure 4.11: Distribution of trapped electron concentration across the thickness (L=500µm) of photoconductor at the end of exposure time with average field, F_0= 1 V/µm

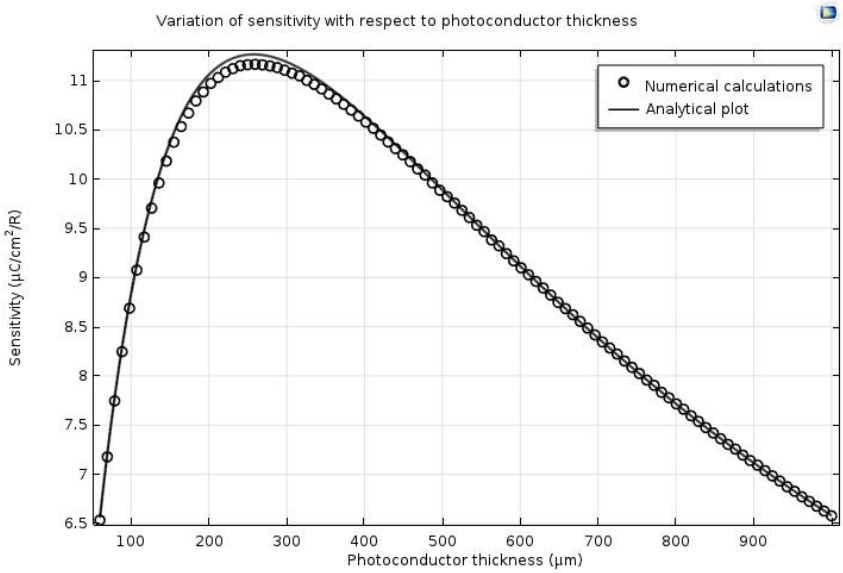

Figure 4.12: Variation of sensitivity versus photoconductor thickness $MAPbI_3$

Charge density is calculated from the current density through the solution of ordinary differential equation (ODE) as in equation (4.11*)*. And the sensitivity is calculated through the formula (4.12*)*.In Figure 4.12, the obtained sensitivity is compared with the standard analytical model as described in [48]. From this comparison, it can be concluded that sensitivity obtained through numerical calculation using COMSOL Multiphysics agrees well with the analytical approach. There exists an optimum thickness that maximizes the sensitivity. This optimum thickness increases with increasing mobility and lifetime.

Figure 4.13 shows the electric field profile variation along the thickness of the detector for different exposure levels. The exposure levels cover the entire range used in chest radiography from 30μR to 3000μR. It is evident that as the exposure level increases the electric field deviates more from the initial value. Furthuremore, the average value of the field is the same as the initial value of electric field.

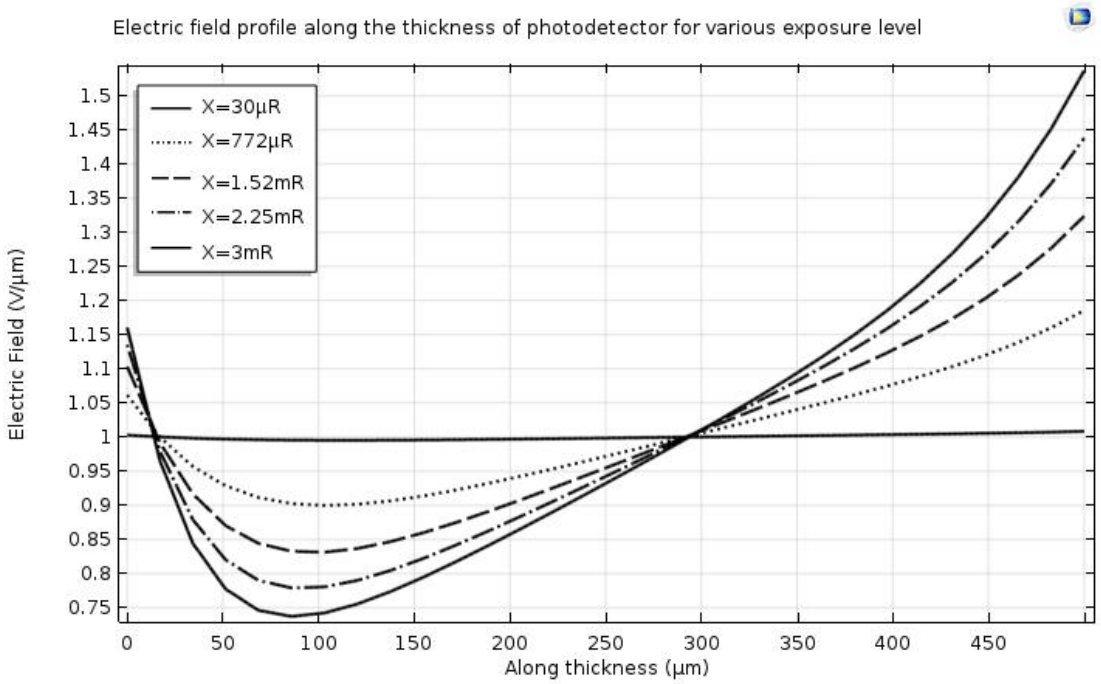

Figure 4.13: Electric field profile along the thickness of detector for various exposure levels (E= 60 keV, F_0= 1 V/μm)

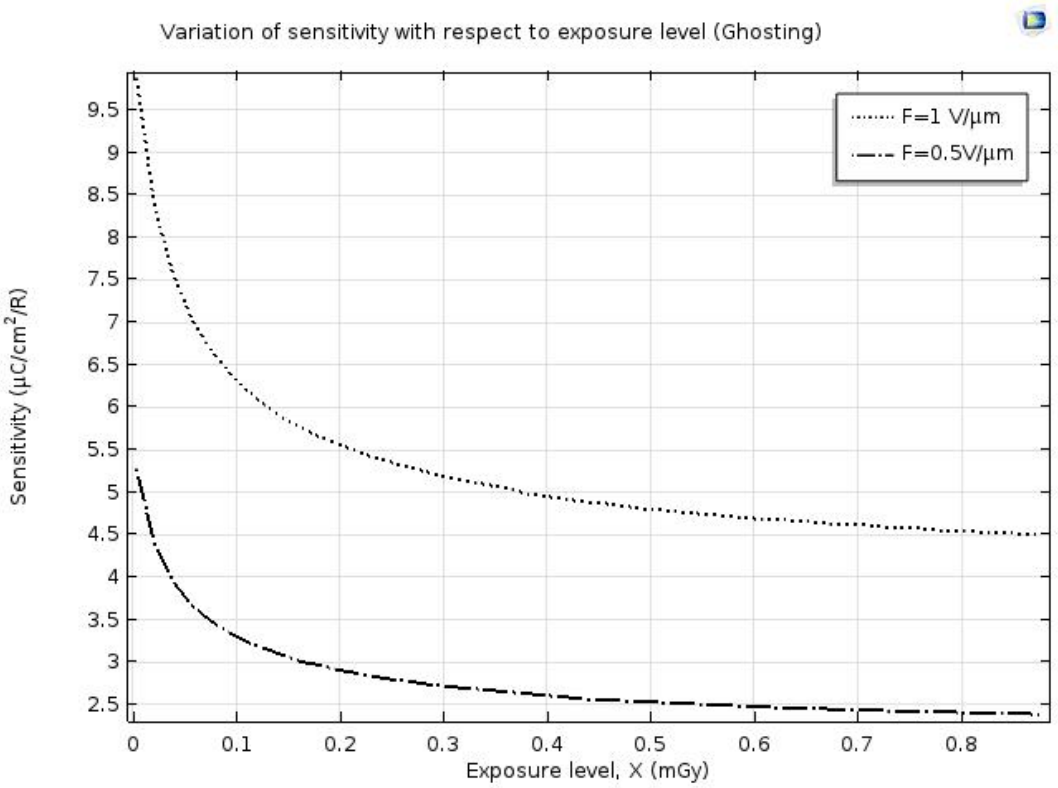

Figure 4.14: Ghosting characteristics of $MAPbI_3$ X-ray photodetector (E=60keV)

Figure 4.14 shows the sensitivity of $MAPbI_3$ photoconductor as a function of exposure for two average electric field. The sensitivity decreases with increasing exposure and rate of reduction decreases with exposure. As a result, the sensitivity may reach a plateau after a very high exposure. The reduction of sensitivity after 1mGy of accumulated exposure is very significant (~53% at F_0=1V/µm, ~49% at F_0=0.5V/µm). The non-uniform electric field and carrier recombination are responsible for this reduction in sensitivity.

Recently, polycrystalline ($MAPbI_3$) perovskite has been investigated with improved fabrication techniques for its characteristics under varying dose [49]. The collected charge density vs dose characteristic deviates from the expected linear behavior as shown in Figure 4.15. The parameters used in Figure 4.15 and Figure 4.16; E=42keV, $W_{\pm}$=4.5eV, L=0.8mm, μ_h= 0.7 cm^2/V-s, μ_e= 0.55 cm^2/V-s, $\tau_h = \tau_e$ = 350 µs, and T_{ex} = 1s. Average incident energy (E) of 42 keV is considered in numerical and analytical calculates which is extracted from the x-ray photon density spectrum [49] with 2.5 mm Al filters and peak emission at 38 keV. It is evident from this fitting that under high exposure levels (X>8mGy) neither the analytical nor numerical calculations catch up with the experimental results. The analytical model shows a linear behavior because it does not

consider bimolecular recombination. Though the numerical model considers all kinds of recombination and shows some nonlinear behavior, still it fails to follow the experimental trend. Two more factor could be responsible such as (i) dose induced generation of new defects and (ii) carrier density dependent free carrier generations.

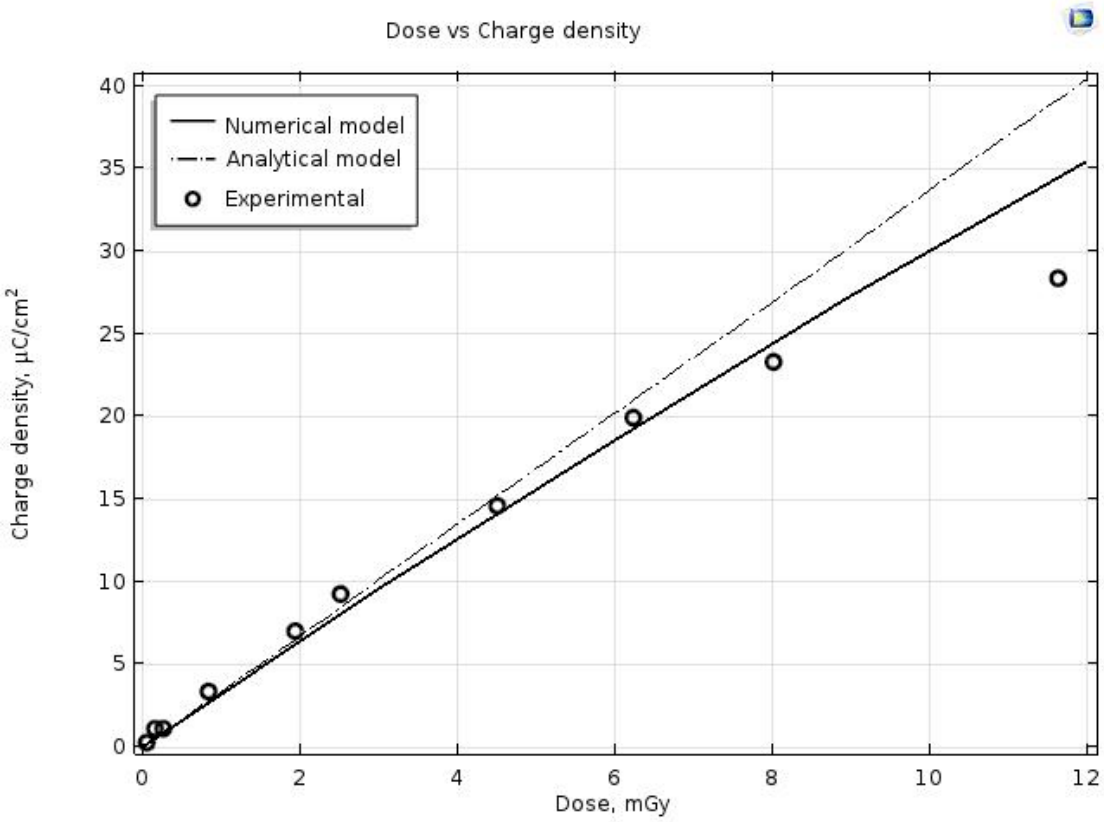

Figure 4.15: Dose vs charge density in $MAPbI_3$ x-ray detector. Experimental data were extracted from [49] (E= 42 keV, F_0= 0.2 V/μm, L= 0.8 mm)

The corresponding variation in the electric field along the thickness of photoconductor is shown as in Figure 4.16.

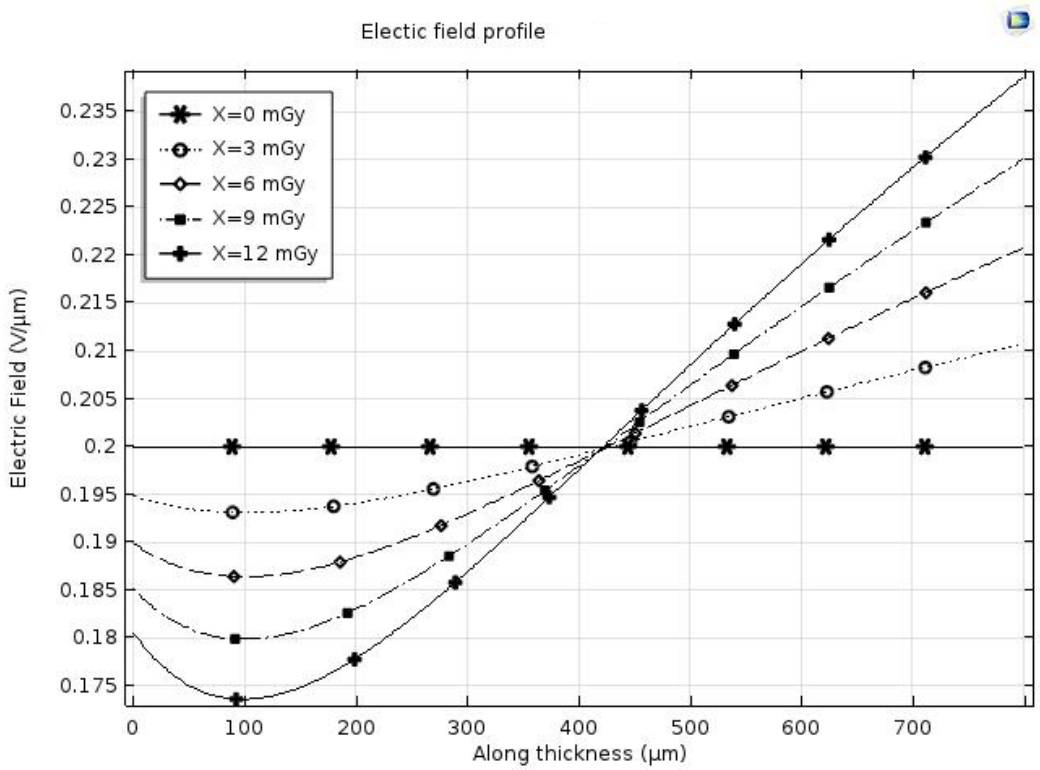

Figure 4.16: Electric field profile along the thickness of photodetector corresponding to Figure 4.15

4.3 Summary

Thus, in this chapter, numerical evaluation of organic perovskite photoconductor is being made. From the comparison with standard analytical models, it becomes evident that analytical results agree well with numerical calculations only at low exposure levels. This is because of the minimum electric field variation at this exposure levels. While the numerical calculations deviate significantly from analytical results at high exposure levels because the significant electric field deviates.

Chapter 5: Conclusion, Contribution, and Future works

5.1 Conclusion

To sum it up, the standard analytical models of sensitivity, photocurrent, dark current (injection limited), Detective Quantum Efficiency (DQE) at zero spatial frequency, and Modulation Transfer Function (MTF) are applied to organic perovskite materials for establishing the underlying mechanism and to assess the quality of signal loss during x-ray imaging. Based upon these models the experimental values are fitted. Numerical investigations are also adopted in this thesis work using COMSOL to exclude the assumption of a constant field in analytical approaches. Furthermore, by numerical calculations, all possible recombination mechanism is included. Hence, the electric field profile across the photoconductor thickness is plotted under illumination of X-rays.

From these works, we conclude, an undesirable photo-gain arises in these materials which are primarily governed by the injection of carriers from the contact terminals. Thus, a need for appropriate blocking contacts with suitable material configurations between different layers of x-ray detector is necessary. This different material configuration must include proper energy alignment between different layer so that any possible charge injection (photo-gain) due to tunneling and band bending can be avoided and the dark currents can be reduced drastically. Although these perovskite materials have better linear attenuation coefficient and X-ray sensitivity than of the a-Se detector, the theoretical MTF $MAPbBr_3$ is like that of the a-Se based detector while $MAPbI_3$ shows worse resolutions. The Detective Quantum Efficiency (DQE) at zero spatial frequency shows a similar result to that of a-Se. Proceeding further, from the ghosting (sensitivity reduction) characteristics of $MAPbI_3$, calculated by the numerical approach, it has been found that under repeated exposure from 300 μR to 100 mR the sensitivity reduces ~53% at F_0=1V/μm, ~49% at F_0=0.5V/μm from its initial value. Towards the end, under high exposure levels, the analytical models do not agree well with the numerical approaches. Hence these analytical models are limited to low exposure levels. This is due to significant variation of an electric field across the thickness of photoconductor and carrier recombination at high exposure levels.

5.2 Contribution

The contribution of this thesis can be summarized below.

- Photo-gain mechanisms in polycrystalline $MAPbI_3$ x-ray imagers are investigated
- Identified the need for structural optimization of x-ray detector with appropriate blocking contacts for low dark current and any possible carrier injection
- Fitting of standard analytical models with experimental results are carried out
- Evaluated the carrier density profile, electric field profile and sensitivity under dynamic conditions through numerical calculations using COMSOL.

The above works resulted in the following publications,

- D. M. Panneerselvam and M. Kabir, "Evaluation of organic perovskite photoconductors for direct conversion X-ray imaging detectors", *Journal of Materials Science: Materials in Electronics*, **vol. 28**, no. 10, pp. 7083-7090, 2017
- D. M. Panneerselvam and M. Z. Kabir, "Numerical evaluation of organic perovskite photoconductors for X-ray image detectors", *The 18th Canadian Semiconductor Science and Technology Conference,* University of Waterloo, Ontario, Canada, August 20-24, 2017. (Accepted)
- D. M. Panneerselvam and M. Z. Kabir, "Performance evaluation of Perovskite Photoconductors for direct conversion X-ray imaging detectors", *The 7th International Conference on Optical, Optoelectronic and Photonic Materials and Applications,* Université de Montréal, Québec, Canada, June 13-17, 2016.

5.3 Future Works

The research on organic perovskite for light harvest has been increasing in recent years because of the superior charge transport properties and low-temperature convenient fabrications. Because of these inherited superiorities, the power conversion efficiency for light harvesting has peaked up to more than 20% within four years of research. Yet there are unresolved queries when organic perovskites are used in X-ray medical imaging. Few researchers tested X-ray sensitivity of their photovoltaic structures and found quite encouraging result. However, a systemic study is vital including the following issues

- A concrete photodetector structure concerning proper blocking contacts along with appropriate energy alignment schemes needs to be developed to reduce the dark currents
- Convenient deposition scheme for large scale deposition of polycrystalline perovskite without affecting the underlying Active Matrix Array (AMA) needs to be addressed
- Although ghosting on organic perovskite photoconductors has been resolved partially in this thesis work, more general idea regarding the ghost recovery of images need to be addressed for organic perovskite
- Detective Quantum Efficiency (DQE) variation with regards to different spatial frequency needs to be addressed.

These ideas can be regarded as the direction for future work on organic perovskite for medical X-ray imaging.

Chapter 6: Reference

[1] "RadiologyInfo.org", *Radiologyinfo.org*,2017. [Online]. Avalable https://www.radiologyinfo.org/. [Accessed: 08- Jun- 2017].

[2] J. A. Rowlands and J. Yorkston, "Flat panel detectors for digital radiography" in *Handbook of Medical Imaging*, vol. 1, J. Beutel, H. L. Kundel, and R. L. Van Metter, Ed. Washington: SPIE, 2000, ch. 4.

[3] S. O. Kasap, M. Z. Kabir and J. Rowlands, "Recent advances in X-ray photoconductors for direct conversion X-ray image detectors", *Current Applied Physics*, **vol. 6**, no. 3, pp. 288-292, 2006.

[4] S. O. Kasap and J. A. Rowlands, "Direct-conversion flat-panel X-ray image detectors," *IEE Proceedings*: *Circuits, Devices, and Systems*, **vol. 149**, no. 2, pp. 85−96, Apr. 2002.

[5] W. Wei, Y. Zhang, Q. Xu, H. Wei, Y. Fang, Q. Wang, Y. Deng, T. Li, A. Gruverman, L. Cao and J. Huang, "Monolithic integration of hybrid perovskite single crystals with heterogenous substrate for highly sensitive X-ray imaging*", Nature Photonics*, **vol. 11**, no. 5, pp. 315-321, 2017.

[6] Z. Song, S. Watthage, A. Phillips and M. Heben, "Pathways toward high-performance perovskite solar cells: review of recent advances in organo-metal halide perovskites for photovoltaic applications", *Journal of Photonics for Energy*, **vol. 6**, no. 2, p. 022001, 2016.

[7] M. Green, A. Ho-Baillie and H. Snaith, "The emergence of perovskite solar cells", *Nature Photonics*, **vol. 8**, no. 7, pp. 506-514, 2014.

[8] A. Chilvery, A. Batra, B. Yang, K. Xiao, P. Guggilla, M. Aggarwal, R. Surabhi, R. Lal, J. Currie and B. Penn, "Perovskites: transforming photovoltaics, a mini-review", *Journal of Photonics for Energy*, **vol. 5**, no. 1, p. 057402, 2015.

[9] C. Zuo, H. Bolink, H. Han, J. Huang, D. Cahen and L. Ding, "Advances in Perovskite Solar Cells", *Advanced Science*, **vol. 3**, no. 7, p. 1500324, 2016.

[10] T. Umebayashi, K. Asai, T. Kondo and A. Nakao, "Electronic structures of lead iodide based low-dimensional crystals", *Physical Review B*, **vol. 67**, no. 15, 2003.

[11] G. Xing, N. Mathews, S. Sun, S. Lim, Y. Lam, M. Gratzel, S. Mhaisalkar and T. Sum, "Long-Range Balanced Electron- and Hole-Transport Lengths in Organic-Inorganic $CH_3NH_3PbI_3$", *Science*, **vol. 342**, no. 6156, pp. 344-347, 2013.

[12] T. Brenner, D. Egger, L. Kronik, G. Hodes and D. Cahen, "Hybrid organic—inorganic perovskites: low-cost semiconductors with intriguing charge-transport properties", *Nature Reviews Materials*, p. 16011, 2016.

[13] K. Domanski, J. Correa-Baena, N. Mine, M. Nazeeruddin, A. Abate, M. Saliba, W. Tress, A. Hagfeldt and M. Grätzel, "Not All That Glitters Is Gold: Metal-Migration-Induced Degradation in Perovskite Solar Cells", *ACS Nano*, **vol. 10**, no. 6, pp. 6306-6314, 2016.

[14] K. Domanski, W. Tress, T. Moehl, M. Saliba, M. Nazeeruddin and M. Grätzel, "Working Principles of Perovskite Photodetectors: Analyzing the Interplay Between Photoconductivity and Voltage-Driven Energy-Level Alignment", *Advanced Functional Materials*, **vol. 25**, no. 44, pp. 6936-6947, 2015.

[15] H. Chen, N. Sakai, A. Jena, Y. Sanehira, M. Ikegami, K. Ho and T. Miyasaka, "A Switchable High-Sensitivity Photodetecting and Photovoltaic Device with Perovskite Absorber", *The Journal of Physical Chemistry Letters*, **vol. 6**, no. 9, pp. 1773-1779, 2015.

[16] T. Moehl, J. Im, Y. Lee, K. Domanski, F. Giordano, S. Zakeeruddin, M. Dar, L. Heiniger, M. Nazeeruddin, N. Park and M. Grätzel, "Strong Photocurrent Amplification in Perovskite Solar Cells with a Porous TiO_2 Blocking Layer under Reverse Bias", *The Journal of Physical Chemistry Letters*, **vol. 5**, no. 21, pp. 3931-3936, 2014.

[17] R. Dong, Y. Fang, J. Chae, J. Dai, Z. Xiao, Q. Dong, Y. Yuan, A. Centrone, X. Zeng and J. Huang, "High-Gain and Low-Driving-Voltage Photodetectors Based on Organolead Triiodide Perovskites", *Advanced Materials*, **vol. 27**, no. 11, pp. 1912-1918, 2015.

[18] J. Li, Z. Nie, H. Li, Y. Peng, Z. Wang, Z. Mai and W. Zheng, "A computational study of tri-s-triazine-based molecules as ambipolar host materials for phosphorescent blue emitters:

effective geometric and electronic tuning", *Journal of Materials Chemistry C*, **vol. 3**, no. 19, pp. 4859-4867, 2015.

[19] C. Kulshreshtha, G. Kim, R. Lampande, D. Huh, M. Chae and J. Kwon, "New interfacial materials for rapid hole-extraction in organic photovoltaic cells", *Journal of Materials Chemistry A*, **vol. 1**, no. 12, p. 4077, 2013.

[20] M. Waqas Alam, Z. Wang, S. Naka and H. Okada, "Mobility enhancement of top contact pentacene based organic thin film transistor with bi-layer GeO/Au electrodes", *Applied Physics Letters*, **vol. 102**, no. 6, p. 061105, 2013.

[21] D. C. Hunt, "Imaging performance of amorphous selenium flat-panel detector for digital fluoroscopy," *SPIE Medical Imaging conference presentation*, San Diego, (2003).

[22] M. Z. Kabir, S. O. Kasap, and J. A. Rowlands, "Photoconductors for X-ray Image Sensors", *Springer Handbook of Electronic and photonic Materials*, Springer Academic Publishers, October 2006 (Chapter 48).

[23] S. Kasap, C. Koughia, J. Berashevich, R. Johanson and A. Reznik, "Charge transport in pure and stabilized amorphous selenium: re-examination of the density of states distribution in the mobility gap and the role of defects", *Journal of Materials Science: Materials in Electronics*, **vol. 26**, no. 7, pp. 4644-4658, 2015.

[24] M. Z. Kabir, "Dark current mechanisms in amorphous selenium-based photoconductive detectors: an overview and re-examination", *Journal of Materials Science: Materials in Electronics*, **vol. 26**, no. 7, pp. 4659-4667, 2015.

[25] S. O. Kasap and J. Rowlands, "Review X-ray photoconductors and stabilized a-Se for direct conversion digital flat-panel X-ray image-detectors", *Journal of Materials Science: Materials in Electronics*, **vol. 11**, no. 3, pp. 179-198, 2000.

[26] S. Yakunin, M. Sytnyk, D. Kriegner, S. Shrestha, M. Richter, G. Matt, H. Azimi, C. Brabec, J. Stangl, M. Kovalenko and W. Heiss, "Detection of X-ray photons by solution-processed lead halide perovskites", *Nature Photonics*, **vol. 9**, no. 7, pp. 444-449, 2015.

[27] H. Wei, Y. Fang, P. Mulligan, W. Chuirazzi, H. Fang, C. Wang, B. Ecker, Y. Gao, M. Loi, L. Cao and J. Huang, "Sensitive X-ray detectors made of methylammonium lead tribromide perovskite single crystals", *Nature Photonics*, **vol. 10**, no. 5, pp. 333-339, 2016.

[28] M. Z. Kabir, "Effects of charge carrier trapping on polycrystalline PbO x-ray imaging detectors", *Journal of Applied Physics*, **vol. 104**, no. 7, p. 074506, 2008.

[29] S. Siddiquee and M. Z. Kabir, "Modeling of photocurrent and lag signals in amorphous selenium x-ray detectors", *Journal of Vacuum Science & Technology A: Vacuum, Surfaces, and Films*, **vol. 33**, no. 4, p. 041514, 2015.

[30] T. Baikie, Y. Fang, J. Kadro, M. Schreyer, F. Wei, S. Mhaisalkar, M. Graetzel and T. White, "Synthesis and crystal chemistry of the hybrid perovskite $(CH_3NH_3)PbI_3$ for solid-state sensitised solar cell applications", *Journal of Materials Chemistry A*, **vol. 1**, no. 18, p. 5628, 2013.

[31] G. Giorgi, J. Fujisawa, H. Segawa and K. Yamashita, "Small Photocarrier Effective Masses Featuring Ambipolar Transport in Methylammonium Lead Iodide Perovskite: A Density Functional Analysis", *The Journal of Physical Chemistry Letters*, **vol. 4**, no. 24, pp. 4213-4216, 2013.

[32] E. Edri, S. Kirmayer, D. Cahen and G. Hodes, "High Open-Circuit Voltage Solar Cells Based on Organic–Inorganic Lead Bromide Perovskite", *The Journal of Physical Chemistry Letters*, **vol. 4**, no. 6, pp. 897-902, 2013.

[33] A. Poglitsch and D. Weber, "Dynamic disorder in methylammoniumtrihalogenoplumbates (II) observed by millimeter-wave spectroscopy", *The Journal of Chemical Physics*, **vol. 87**, no. 11, pp. 6373-6378, 1987.

[34] "X-Ray and Gamma-Ray Data", *NIST*, 2017. [Online]. Available: https://www.nist.gov/node/428981. [Accessed: 12- Mar- 2017].

[35] J. Beutel, H. L. Kundel and R. L. Van Metter (eds.) *Handbook of Medical Imaging*, (SPIE Press, Washington, 2000), p. 31.

[36] M. Z. Kabir, E. Emelianova, V. Arkhipov, M. Yunus, S. O. Kasap and G. Adriaenssens, "The effects of large signals on charge collection in radiation detectors: Application to amorphous selenium detectors", *Journal of Applied Physics*, **vol. 99**, no. 12, p. 124501, 2006.

[37] S. O. Kasap, "X-ray sensitivity of photoconductors: application to stabilized a-Se", *Journal of Physics D: Applied Physics*, **vol. 33**, no. 21, pp. 2853-2865, 2000.

[38] C. Klein, "Bandgap Dependence and Related Features of Radiation Ionization Energies in Semiconductors", *Journal of Applied Physics*, **vol. 39**, no. 4, pp. 2029-2038, 1968.

[39] S. O. Kasap, M. Z. Kabir and J. Rowlands, "Recent advances in X-ray photoconductors for direct conversion X-ray image detectors", *Current Applied Physics*, **vol. 6**, no. 3, pp. 288-292, 2006.

[40] R. Dong, Y. Fang, J. Chae, J. Dai, Z. Xiao, Q. Dong, Y. Yuan, A. Centrone, X. Zeng and J. Huang, "High-Gain and Low-Driving-Voltage Photodetectors Based on Organolead Triiodide Perovskites", *Advanced Materials***, vol. 27**, no. 11, pp. 1912-1918, 2015.

[41] M. Z. Kabir, M. W. Rahman, and W. Y Shen, "Modelling of DQE of direct conversion X-ray imaging detectors incorporating charge carrier trapping and K-fluorescence," *IET Circuits Devices and Systems*, **vol. 5**, pp. 222-231, 2011.

[42] M. Z. Kabir and S. O. Kasap, "DQE of photoconductive x-ray image detectors: application to a-Se", *Journal of Physics D: Applied Physics*, **vol. 35**, no. 21, pp. 2735-2743, 2002.

[43] W. Que and J. Rowlands, "X-ray imaging using amorphous selenium: Inherent spatial resolution", *Medical Physics*, **vol. 22**, no. 4, pp. 365-374, 1995.

[44] M. Z. Kabir and S. O. Kasap, "Modulation transfer function of photoconductive X-ray image detectors: effects of charge carrier trapping," J*ournal of Physics D: Applied Physics*, **vol. 36**, pp. 2352-2358, 2003.

[45] M. Z. Kabir, S.O. Kasap, W. Zhao, and J.A. Rowlands, "Direct conversion X-ray sensors: Sensitivity, DQE & MTF," *IEE Proceedings-CDS: Special Issue on Amorphous and Microcrystalline Semiconductors*, **vol. 150**, pp. 258-266, 2003.

[46] **D. M. Panneerselvam** and M. Z. Kabir, "Evaluation of organic perovskite photoconductors for direct conversion X-ray imaging detectors", *Journal of Materials Science: Materials in Electronics*, **vol. 28**, no. 10, pp. 7083-7090, 2017.

[47] Hassan Naimul, and Shaikh Asif Mahmood. "X-ray sensitivity of poly (triarylamine)(PTAA)." *Telecommunications and Photonics (ICTP)*, 2015 IEEE International Conference on. IEEE, 2015.

[48] M. Z. Kabir and S. O. Kasap, "Charge collection and absorption-limited sensitivity of x-ray photoconductors: Applications to a-Se and HgI_2", *Applied Physics Letters*, **vol. 80**, no. 9, pp. 1664-1666, 2002.

[49] S. Shrestha, R. Fischer, G. Matt, P. Feldner, T. Michel, A. Osvet, I. Levchuk, B. Merle, S. Golkar, H. Chen, S. Tedde, O. Schmidt, R. Hock, M. Rührig, M. Göken, W. Heiss, G. Anton and C. Brabec, "High-performance direct conversion X-ray detectors based on sintered hybrid lead triiodide perovskite wafers", *Nature Photonics*, **vol. 11**, no. 7, pp. 436-440, 2017.